Article

Diagnosis of the σ-, π- and $(\sigma+\pi)$-Aromaticity by the Shape of the NICS$_{zz}$-Scan Curves and Symmetry-Based Selection Rules

Athanassios C. Tsipis [1,*]**, Ioannis G. Depastas** [2] **and Constantinos A. Tsipis** [2]

[1] Laboratory of Inorganic and General Chemistry, Department of Chemistry, University of Ioannina, 451 10 Ioannina, Greece

[2] Laboratory of Applied Quantum Chemistry, Faculty of Chemistry, Aristotle University of Thessaloniki, 541 24 Thessaloniki, Greece; E-Mails: idepast@chem.auth.gr (I.G.D.); tsipis@chem.auth.gr (C.A.T.)

* Author to whom correspondence should be addressed; E-Mail: attsipis@uoi.gr

Abstract. The NICS$_{zz}$-scan curves of aromatic organic, inorganic and "all-metal" molecules in conjunction with symmetry-based selection rules provide efficient diagnostic tools of the σ-, π- and/or double $(\sigma + \pi)$-aromaticity. The NICS$_{zz}$-scan curves of σ-aromatic molecules are symmetric around the z-axis, having half-band widths approximately less than 3 Å with the induced diatropic ring current arising from $T_{x,y}$-allowed transitions involving exclusively σ-type molecular orbitals. Broad NICS$_{zz}$-scan curves (half-band width approximately higher than 3 Å) characterize double $(\sigma + \pi)$-aromaticity, the chief contribution to the induced diatropic ring current arising from $T_{x,y}$-allowed transitions involving both σ- and π-type molecular orbitals. NICS$_{zz}$-scan curves exhibiting two maxima at a certain distance above and below the molecular plane are typical for $(\sigma + \pi)$-aromatics where the π-diatropic ring current overwhelms the σ-type one. In the absence of any contribution from the σ-diatropic ring current, the NICS$_{zz}(0)$ value is close to zero and the molecule exhibits pure π-aromaticity.

Keywords: aromaticity; delocalization; σ-, π-, $(\sigma+\pi)$-aromaticity; NICS$_{zz}$-scan; density functional theory (DFT)

1. Introduction

The collection of recent reviews in the topic of aromaticity/antiaromaticity [1-9] shows a rather large consensus appear in the computation or experimental tests for the diagnosis of the aromaticity/antiaromaticity (structural, electronic, magnetic, thermodynamic and kinetic diagnostic tools) whereas the mechanisms themselves still remain open to the debate. Various criteria have been used to judge aromaticity/antiaromaticity, but no one is satisfactory, particularly in predicting the orbital type (*s*-, *p*-, *d*-, *f*-orbital) of aromaticity [10]. Among the usual diagnostic probes of aromaticity/antiaromaticity developed so far those based on the dynamic magnetic measurements, in particular the Nucleus Independent Chemical Shifts (NICS) was the most widely used as a quantitative measure for aromaticity [11-13]. The NICS index is the negative value of the isotropic magnetic shielding computed at chosen points in the vicinity of molecules and, hence, directly related to the shielding function. It is typically computed at ring centers, at points above, and even on grids [14] in and around the molecule. The NICS criterion continues to be enhanced and refined, with the out-of-plane zz-components of the shielding tensor elements $NICS_{zz}(0)$ and $NICS_{zz}(1)$ proposed to be a superior aromaticity descriptor [15,16]. Furthermore, the CMO-NICS criterion [17-19] of aromaticity dissects the total shieldings calculated at ring or cage centers, into individual contributions from each canonical molecular orbital (CMO).

It was also established that the shapes of the NICS-scan profiles provide a clear picture of the type of the ring current in aromatic and antiaromatic systems [20,21] and can be used to characterize unequivocally whether an inorganic system is aromatic, non-aromatic and antiaromatic [22,23]. The reliability of the NICS-scan scheme in assessing aromatic behavior of some planar six-membered heteroaromatic systems has been explored recently by Seal and Chakrabarti [24]. These authors using homodesmotic reactions, aromatic stabilization energy (ASE) and NICS-scan to assess aromaticity of several systems concluded that homodesmotic reactions and NICS-scan agree for all systems but ASE does not for some of them. Morao and Cossio [25] introduced a simple ring current model to characterize the in-plane σ- and out-of-plane π-aromaticity in pericyclic reactions. In-plane aromaticity exhibits a maximum diamagnetic shielding σ_{zz}^{d} at the ring center, while π-aromaticity exhibits two ring currents moving at a certain distance above and below the molecular plane. The σ-π separation in all metal aromatic and antiaromatic systems has critically been examined and computational strategies to unambiguously determine the aromaticity/antiaromaticity characteristics of such clusters have been presented by Pati *et al*. [26-29].

On the other hand, simple symmetry-based selection rules derived from group theory helped rationalize and predict ring currents to classify π systems [30-33]. Plotting of current-density maps was also suggested as a standard tool for the resolution of debates about aromaticity and for the interpretation of calculated chemical shift values [30-32,34-36]. Sundholm and coworkers [37-39] introduced the aromatic ring current shielding (ARCS) method to determine the strength of the induced ring current and consequently the relative degree of aromaticity in aromatic systems. In addition, they applied the gauge-including magnetically induced current (GIMIC) method to $[c\text{-}Al_4]^{2-}$ and $[c\text{-}Al_4]^{4-}$ clusters to elucidate the type of aromaticity in these aromatics [37-39]. Heine *et al*. [40,41] represented graphically with three-dimensional isosurfaces the induced magnetic field of cyclic molecules and showed that the appearance of the magnetic response characterizes aromatic, antiaromatic and non-

aromatic molecules. They also showed that the z-component of the induced magnetic field is directly connected to NICS$_{zz}$. Finally, the recently developed Anisotropy of the Current Induced Density (ACID) mapping was suggested as a better probe of aromaticity [42,43].

Recently, we showed that the NICS$_{zz}$-scan curves in conjunction with symmetry-based selection rules for the lowest translationally- and rotationally-allowed transitions help rationalize and predict the orbital-type of aromaticity/antiaromaticity in magnetoresponsive three-membered rings of *d*- and *f*-block elements [44], and unequivocally probe the antiaromaticity in a wide range of antiaromatic organic and inorganic rings/cages [45]. Therefore, we thought it would be advisable to test the efficiency of the NICS$_{zz}$-scan profiles in conjunction with symmetry-based selection rules to provide a clear picture of the orbital type (*s*-, *p*-, *d*-, *f*-orbital) of aromaticity in a wide range of aromatic organic and inorganic molecules, proving its general use as a powerful diagnostic tool of the orbital type of aromaticity/antiaromaticity. To achieve this goal, we calculated the NICS$_{zz}$-scan profiles of a wide range of aromatic organic and inorganic molecules, whose magnetic-response properties have been exhaustively investigated and well-characterized in the framework of the aromaticity concept. The results obtained are thoroughly analyzed and presented herein.

2. Computational Details

In view of the good performance of density functional theory (DFT), we were inclined to use DFT calculations on the compounds we studied using the GAUSSIAN03 program suite [46]. The geometries of all species were fully optimized at the B3LYP level, using 6-311+G(d,p) basis set for all elements, except those of the fifth and sixth row elements for which the SDD basis set was used [47,48]. Full geometry optimization was performed for each structure using Schlegel's analytical gradient method [49], and the attainment of the energy minimum was verified by calculating the vibrational frequencies that result in the absence of imaginary eigenvalues. All the stationary points were identified for minimum (number of imaginary frequencies NIMAG=0) or transition states (NIMAG=1). Magnetic shielding tensors were computed with the GIAO (gauge independent atomic orbitals) DFT method [50,51] as implemented in the GAUSSIAN03 series of programs [46] employing the B3LYP level of theory. Nucleus-Independent Chemical Shifts (NICS) were computed at the B3LYP level according to the procedure described by Schleyer *et al.* [11]. The computational protocol used is that applied in the previous studies of the aromaticity/antiaromaticity of most of the aromatic molecules discussed herein. The contribution to the induced ring current from the σ- and π-type diatropic and or paratropic translationally (T$_{x,y}$) and rotationally (R$_z$) allowed transitions was inferred from the estimated excitation energies based on symmetry and energy criteria. For a planar conjugated molecule in which the ring currents are induced by a magnetic field perpendicular to the molecular plane, three factors will determine the existence and strength of the contribution of an occupied-to-unoccupied orbital transition, $\psi_n \rightarrow \psi_p$ transition, namely symmetry, spatial distribution and energy. Symmetry determines whether a $\psi_n \rightarrow \psi_p$ transition contributes at all to the current density, spatial distribution of the orbitals determines whether an allowed transition moment will be large or small and the difference in orbital energies (excitation energies) affects the relative weight of a given transition moment in the total induced ring current. Thus, a $\psi_n \rightarrow \psi_p$ transition makes a conventionally *diamagnetic* (*diatropic*) contribution to current density if the direct product of representations $\Gamma(\psi_n)\times$

$\Gamma(\psi_p) \times \Gamma(T_x, T_y)$ contains a totally symmetric component, and a conventionally *paramagnetic* (*paratropic*) contribution to current density if the direct product $\Gamma(\psi_n) \times \Gamma(\psi_p) \times \Gamma(R_z)$ contains a totally symmetric component. A mixed contribution results if both direct products have a totally symmetric component, while no contribution results if neither direct product has a totally symmetric component [30-32].

3. Results and Discussion

3.1.   The NICS$_{zz}$-scan profiles of 2e- and 6e-σ-aromatics

Let us first examine the shape and most salient features of the NICS$_{zz}$-scan profiles of 2e- and 6e-σ-aromatics, the $[c\text{-}H_3]^+$ and c-H$_6$ species being the prototypes [52-55]. It should be noted that the optimized structures of the $[c\text{-}H_4]^{2-}$, $[c\text{-}H_5]^-$ and $[c\text{-}H_6]$ clusters were obtained under symmetry constrains and correspond to third, second and first order saddle points, respectively. The optimized D_{nh} symmetric $[c\text{-}H_x]^q$ aromatic rings are similar to the optimized structures reported previously [52-55]. The NICS$_{zz}$-scan profiles of selected 2e- and 6e-σ-aromatics are visualized in Figure 1, while the main features of the NICS$_{zz}$-scan curves along with the R_{av} values, e.g. the average distance of the ring current to the center of the ring, are compiled in Table 1.

Figure 1. NICS$_{zz}$-scan profiles (NICS$_{zz}$ in ppm, R in Å) of selected 2e-σ- and 6e-σ-aromatics computed at the B3LYP/6-311+G(d,p) level.
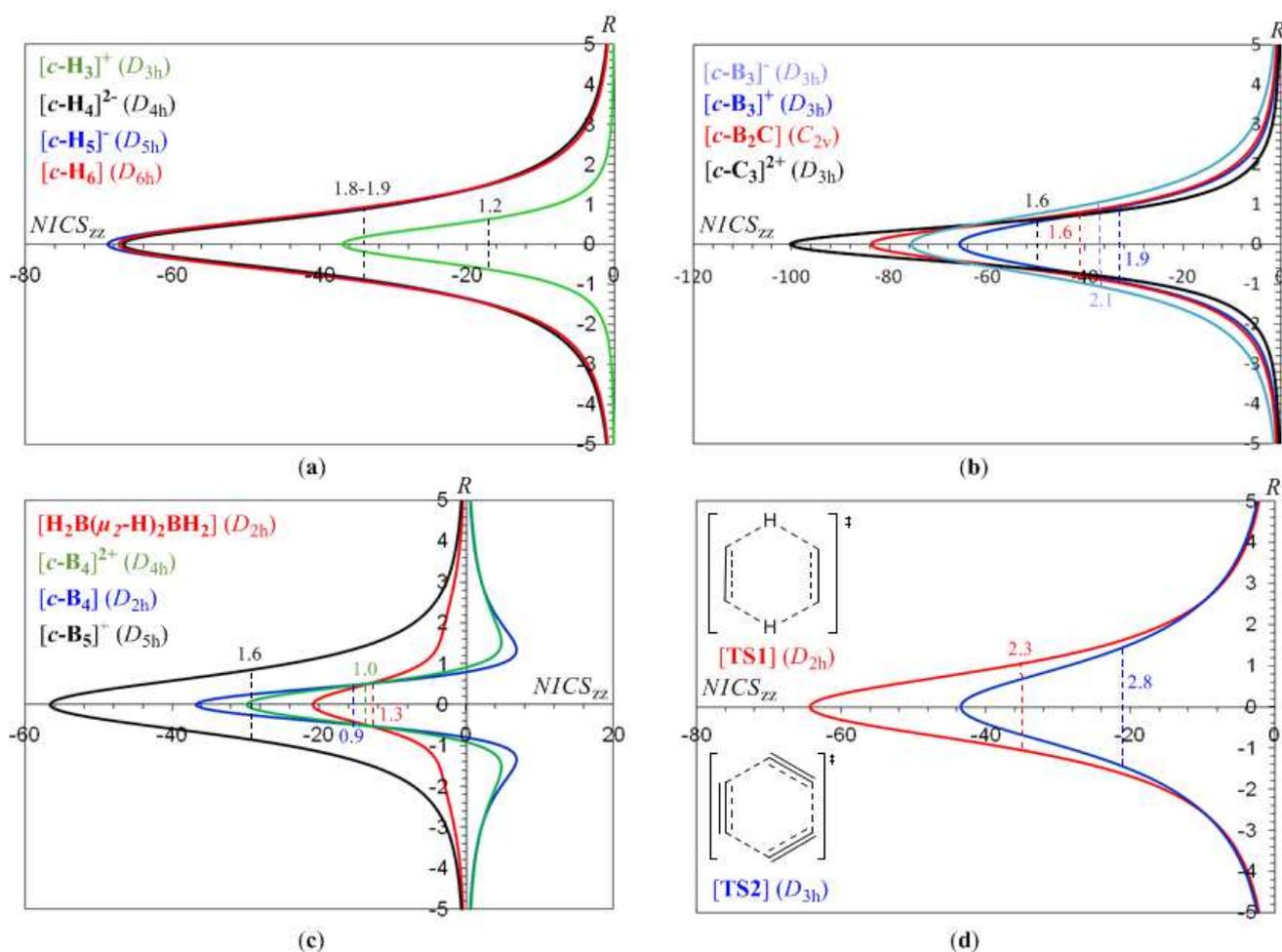
Table 1. The NICS values (in ppm) calculated at the ring center, NICS(0) and 1.0 Å above the ring center, NICS(1), the zz-component of the shielding tensor elements, NICS$_{zz}$(0) and NICS$_{zz}$(1) along with the half-band width of the NICS$_{zz}$-scan curves (in Å) and R_{av} (in Å) for selected σ-aromatic molecules computed at the B3LYP/6-311+G(d,p) level.

Compound	NICS(0)	NICS(1)	NICS$_{zz}$(0)	NICS$_{zz}$(1)	Half-band width	R_{av}
$[c\text{-}H_3]^+$ (D_{3h})	-33.5	-1.9	-36.9	-7.9	1.2	0.509
$[c\text{-}H_4]^{2-}$ (D_{4h})	-16.0	-8.9	-66.8	-29.7	1.8	0.701
$[c\text{-}H_5]^-$ (D_{5h})	-20.1	-9.4	-68.9	-30.5	1.8	0.843
$[c\text{-}H_6]$ (D_{6h})	-24.1	-10.0	-67.4	-31.1	1.9	0.992
$[c\text{-}B_3]^-$ (D_{3h})	-73.6	-28.2	-75.6	-39.3	2.1	0.467
$[c\text{-}B_3]^+$ (D_{3h})	-65.4	-17.3	-65.7	-30.3	1.9	0.480
$[c\text{-}B_2C]$ (C_{2v})	-80.1	-22.6	-83.8	-31.6	1.6	0.438
$[c\text{-}C_3]^{2+}$ (D_{3h})	-95.0	-16.3	-100.3	-25.6	1.2	0.349
$[c\text{-}B_4]$ (D_{2h})	-35.7	-9.2	-36.8	4.7	0.9	0.647
$[c\text{-}B_4]^{2+}$ (D_{4h})	-28.8	-3.4	-29.9	1.5	1.0	0.698
$[H_2B(\mu_2\text{-}H)_2BH_2]$ (D_{2h})	-26.0	-3.2	-20.8	-6.1	1.3	0.717
$[c\text{-}B_5]^+$ (D_{5h})	-36.2	-18.8	-56.6	-24.3	1.6	0.896
TS1^a (D_{2h})	-27.8	-13.3	-64.4	-36.7	2.3	0.918
TS2^b (D_{3h})	-17.6	-10.2	-43.5	-28.6	2.8	1.382
$[c\text{-}Li_3]^+$ (D_{3h})	-11.1	-6.8	-8.7	-7.3	3.7	1.704
$[c\text{-}C_3H_6]$ (D_{3h})	-42.7	-8.6	-29.8	-24.2	3.2	0.518

[a] TS1 = transition state for the concerted transfer of two hydrogen atoms from ethane to ethylene (double group transfer reactions). [b] TS2 = transition state for the trimerization of acetylene to form benzene.

The half-band width, e.g., the width of the symmetric curve at half the NICS$_{zz}$ value, of the NICS$_{zz}$-scan curves depends on the ring radius, R_{av}, evaluated as $R_{av} = \dfrac{1}{n}\sum_{i=1}^{n} R_i$, where n is the number of the nuclei of the ring, and R_i is the distance from the ring center to the nucleus i. For the rings where the 2p orbitals (*radial* 2p orbitals) participate also in the bonding, forming molecular orbitals contributing to the diatropic ring current of the σ-aromatics, R_{av} was evaluated as $R_{av} = \dfrac{1}{n}\sum_{i=1}^{n}\left(R_i - \dfrac{4}{Z_i}a_0\right)$, where Z_i is the atomic number of the i-atom, and a_0 is the Bohr radius. The term $4a_0/Z_i$ corresponds to the maximum of the probability of the radial function $4\pi r^2 R_{n,l}{}^2(\mathbf{r})$ for a 2p atomic orbital.

It can be seen that the NICS$_{zz}$-scan curves are symmetric around the z-axis with the NICS$_{zz}$ values decaying rapidly and monotically with respect to R. The half-band widths of the NICS$_{zz}$-scan curves for the σ-aromatics exhibiting s-orbital aromaticity range from 1.2 to 1.9 Å (R_{av} ranging from 0.509 to 0.992 Å) is characteristic of the in-plane pure σ-aromaticity due to cyclic delocalization of two 1s electrons over the three-membered ring in $[c\text{-}H_3]^+$ and six 1s electrons over the four-, five- and six-membered rings in $[c\text{-}H_4]^{2-}$, $[c\text{-}H_5]^-$ and $[c\text{-}H_6]$. Analogous symmetric sharp NICS$_{zz}$-scan curves with half-band widths in the range of 0.9 to 2.1 Å are obtained for the $[c\text{-}B_3]^-$, $[c\text{-}B_3]^+$, $[c\text{-}B_2C]$, $[c\text{-}C_3]^{2+}$, $[c\text{-}B_4]$, $[c\text{-}B_4]^{2+}$, $[c\text{-}B_5]^+$ (Figure 1b,c), as well as for the transition states TS1 and TS2 (Figure 1d) of the

concerted transfer of two hydrogen atoms from ethane to ethylene (double group transfer reactions) and the trimerization of acetylene to form benzene respectively. shown in Scheme I. The latter two NICS$_{zz}$-scan curves have a slightly larger half-band width of 2.3 and 2.8 Å, respectively.

Scheme I. The transition states TS1 and TS2 of the concerted transfer of two hydrogen atoms from ethane to ethylene and the trimerization of acetylene to form benzene, respectively.
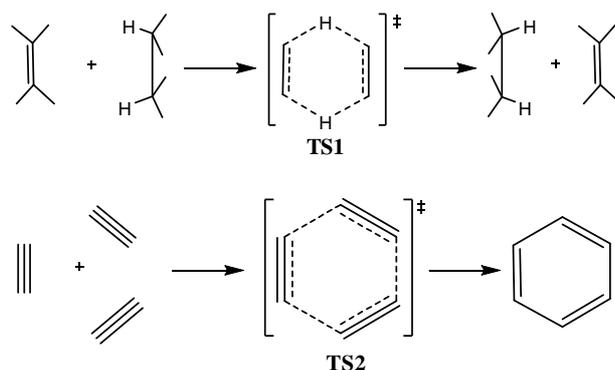
3.2. Magnetotropicity of the 2e- and 6e-σ-aromatics

In the $[c\text{-}H_3]^+$ species with D_{3h} symmetry, the chief contribution to induced diatropic ring current arises from the $T_{x,y}$-allowed HOMO (a_1') → LUMO (e') transition with excitation energy 18.74 eV. In the $[c\text{-}H_4]^{2-}$ (D_{4h}) cluster the chief contribution to induced diatropic ring current arises from the $T_{x,y}$-allowed HOMO,-1 (e_u) → LUMO (b_{1g}) and HOMO,-1 (e_u) → LUMO+1 (a_{1g}) transitions having excitation energies 6.33 and 6.77 eV respectively (notice that HOMO,-1 denotes HOMO and HOMO-1, LUMO+1,+2 denotes LUMO+1 and LUMO+2, *etc.*). In the $[c\text{-}H_5]^-$ (D_{5h}) cluster the chief contribution to induced diatropic ring current arises from the $T_{x,y}$-allowed HOMO,-1 (e_1') → LUMO+2 (a_1') with excitation energy 11.02 eV. Finally, in the $[c\text{-}H_6]$ (D_{6h}) cluster the chief contribution to induced diatropic ring current arises from the $T_{x,y}$-allowed HOMO,-1 (e_{1u}) → LUMO+2 (a_{1g}) with excitation energy 14.14 eV. The higher excitation energy of the $T_{x,y}$-allowed transition in the $[c\text{-}H_3]^+$ cluster accounts well for the weaker aromatic character. It should be noted that all orbitals involved in the $T_{x,y}$-allowed transitions responsible for the induced diatropic ring current are σ-type MOs.

In the $[c\text{-}B_3]^-$ and $[c\text{-}C_3]^{2+}$ species with D_{3h} symmetry, the $T_{x,y}$-allowed HOMO (a_1') → LUMO+1,+2 (e') excitations with excitation energies 3.42 and 4.25 eV respectively are responsible for the induced diatropic ring current. On the other hand, for the $[c\text{-}B_3]^+$ species the $T_{x,y}$-allowed HOMO,-1 (e') → LUMO (a_1') excitation with excitation energy 4.16 eV contributes primarily to the induced diatropic ring current. The lower magnetic aromaticity of the $[c\text{-}B_3]^+$ species compared to that of the $[c\text{-}B_3]^-$ 2e-σ-aromatic could be explained by the higher energy difference between the orbitals involved in the respective excitations (4.16 *versus* 3.42 eV). Both the e' and a_1' MOs participating in the $T_{x,y}$-allowed transitions are σ-type MOs and are primarily responsible for the σ-aromaticity of the $[c\text{-}B_3]^-$ .and $[c\text{-}B_3]^+$ species. The $1a_2''$ bonding HOMO-1 in $[c\text{-}B_3]^-$ and $[c\text{-}C_3]^{2+}$ and HOMO in $[c\text{-}B_3]^+$ constructed from the overlap of the $2p_z$ AOs of the ring atoms, being a pure π-bonding MO similar to the π-MO in the cyclopropenyl cation ($[c\text{-}C_3H_3]^+$), is magnetically inactive and therefore cannot

contribute to the induced diatropic ring current. The magnetic inactivity of the $1a_2''$ π-MO is further confirmed from the NICS$_{zz}$-scan profile of the putative $[c\text{-}B_3]^{3+}$ species where, due to the removal of two electrons, the $1a_2''$ π-MO is vacant. The computed NICS$_{zz}$(0) and NICS$_{zz}$(1) values for the $[c\text{-}B_3]^{3+}$ species are -50.7 and -6.3 ppm, respectively, while the half-band width is 1.0 Å. However, the higher NICS$_{zz}$(0) value of the $[c\text{-}B_3]^+$ species by 15.0 ppm compared to that of the $[c\text{-}B_3]^{3+}$ one is probably indicative for a small contribution of the $1a_2''$ π-MO to the diatropic ring current as well, supported by the T$_{x,y}$-allowed transitions HOMO-1 (a_2'') $\rightarrow$ LUMO+5,+6 (e'') in $[c\text{-}B_3]^-$, HOMO (a_2'') $\rightarrow$ LUMO+3,+4 (e'') in $[c\text{-}B_3]^+$ and HOMO-1 (a_2'') $\rightarrow$ LUMO+2,+3 (e'') in $[c\text{-}C_3]^{2+}$ having relatively high excitation energies of 5.97, 8.77 and 11.20 eV, respectively. As the contribution of the $1a_2''$ π-MO to the diatropic ring current giving rise to π-aromaticity is small, the NICS$_{zz}$-scan curve is still narrow with band width less than 3.0 Å. Boldyrev and co-workers [56-58] have identified $[c\text{-}B_3]^-$ as 2+2 doubly aromatic system containing a π-type $(1a_2'')$ HOMO-1 and radial σ-type $(2a_1')$ HOMO both molecular orbitals contributing to the induced diatropic ring current. The NICS$_{zz}$-scan curve of the $[c\text{-}B_3]^-$ species in conjunction with symmetry-based selection rules are in support of the double aromaticity, but with the induced π-diatropic ring current much weaker than the dominant induced σ-diatropic ring current. In effect the canonical orbital contributions to the out-of-plane NICS tensor component (CMO-NICS$_{zz}$) for the $[c\text{-}B_3]^-$ species estimated to be -16.1 ppm from the HOMO-4 $(1a_1')$, -36.0 ppm from the degenerate HOMO-2,-3 $(1e')$, -11.5 ppm from the HOMO-1 $(1a_2'')$, the π-type MO and -11.7 ppm from the HOMO $(2a_1')$ clearly illustrate the much weaker induced π-diatropic ring current (-11.5 ppm) than the dominant σ-diatropic ring current (-63.8 ppm). Therefore, the $[c\text{-}B_3]^-$ species could be considered practically as a σ-aromatic species. Similarly, the estimated CMO-NICS$_{zz}$ values for the $[c\text{-}B_3]^+$ species found to be -16.6 ppm from the HOMO-3 $(1a_1')$, -37.2 ppm from the degenerate HOMO-1,-2 $(1e')$ and only -12.3 ppm from the π-type HOMO $(1a_2'')$. Compare again the much weaker induced π-diatropic ring current (-12.3 ppm) than the dominant σ-diatropic ring current (-53.8 ppm). Finally, the estimated CMO-NICS$_{zz}$ values for the putative $[c\text{-}B_3]^{3+}$ species found to be -18.1 ppm from the HOMO-1 $(1a_1')$ and -31.2 ppm from the degenerate HOMO,-1 $(1e')$ contribute exclusively to the induced σ-diatropic ring current. Notice that the $1a_1'$ and $1e'$ bonding and nonbonding MOs respectively are formed primarily from the overlap of the filled $2s$ AOs of the boron atoms. It can be concluded that the CMO-NICS$_{zz}$ analysis data reinforce the efficiency of the NICS$_{zz}$-scan curves and symmetry-based rules model to diagnose the orbital type of aromaticity of the aforementioned 2e- and 6e-σ-aromatics.

In the $[c\text{-}B_4]$ (D_{2h}) molecule the T$_{x,y}$-allowed transitions contributing to the induced diatropic ring current are the HOMO-2 (b_{3u}) $\rightarrow$ LUMO (a_g), HOMO-3 (b_{2u}) $\rightarrow$ LUMO (a_g) and HOMO (a_g) $\rightarrow$ LUMO+4 (b_{2u}) excitations with excitation energies 4.58, 6.93 and 6.96 eV respectively. In addition the R$_z$-allowed HOMO (a_g) $\rightarrow$ LUMO+3 (b_{1g}) transition with excitation energy 6.27 eV contributes to the long range induced paratropic ring current (Figure 1c). The same holds true for the $[c\text{-}B_4]^{2+}$ (D_{4h}) dicationic species where the T$_{x,y}$-allowed transitions contributing to the induced diatropic ring current are the HOMO-2,-3 (e_u) $\rightarrow$ LUMO (a_{1g}) and HOMO (a_{2u}) $\rightarrow$ LUMO+2,+3 (e_u) excitations with excitation energies 6.26 and 6.36 eV, respectively, while the R$_z$-allowed HOMO-1 (b_{2g}) $\rightarrow$ LUMO+1 (b_{1g}) transition with excitation energy 5.25 eV contributes to the long range induced paratropic ring current. Finally, in the $[c\text{-}B_5]^+$ (D_{5h}) molecule the T$_{x,y}$-allowed transitions contributing to the induced

diatropic ring current are the HOMO-1 (a_2'') $\rightarrow$ LUMO,+1 (e_1'') and HOMO (a_1') $\rightarrow$ LUMO+2,+3 (e_1') excitations with excitation energies 4.86 and 4.96 eV, respectively.

It is important to note that the dominant contribution to aromaticity of the aforementioned σ-aromatics due to the in-plane σ-MOs constructed from the overlap of the $2s$ and/or $2p$ AOs of the ring atoms is nicely reflected on the excellent linear correlation of the NICS$_{zz}$(0) with the R_{av} of the rings (Figure 2).

Figure 2. Linear relationship between NICS$_{zz}$(0) (ppm) and R_{av} (Å) for σ-aromatic molecules with radial in-plane σ-MOs of Hückel topology constructed from the overlap of the $2p$ AOs of the ring atoms.
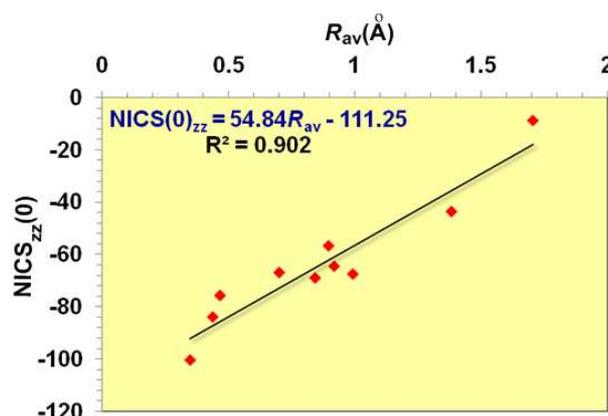
In-plane aromaticity is a general feature of transition states associated with pericyclic reactions [25,56-58]. Cossio *et al*. [25] using a simple ring current model based on the NICS-scan profiles of the transition states was able to characterize the in-plane and π-aromaticity. For the transition states exhibiting in-plane aromaticity the NICS-scan curves showed a maximum at the molecular plane and decaying rapidly above and below of such plane. In contrast, in π-aromatic systems the NICS-scan curves showed a maximum at a certain distance above and below the molecular plane, which corresponds to the covalent radii of the involved atoms. The shapes of the NICS$_{zz}$-scan curves of the transition states TS1 and TS2 for the concerted transfer of two hydrogen atoms from ethane to ethylene (double group transfer reactions) [59] and the trimerization of acetylene to form benzene [60,61] respectively (Figure 1d), provide a clear evidence for their in-plane σ-aromatic character. Indeed the NICS$_{zz}$-scan curves are symmetric sharp curves with half-band widths less than 3 Å.

The predictive power of the NICS$_{zz}$-scan curves on the orbital type of aromaticity was further corroborated by exploring the orbital type of aromaticity of the $[c\text{-}B_3H_7]^{2-}$ (C_s) [62] and $[c\text{-}B_3(\mu_2\text{-}P)_3]^{2-}$ (D_{3h}) σ-aromatics, both involving a three-membered B_3 ring. Indeed for both species the NICS$_{zz}$-scan curves are symmetric sharp curves with half-band widths of 1.6 and 1.8 Å, respectively. The computed NICS$_{zz}$(0), NICS$_{zz}$(1) values of the $[c\text{-}B_3H_7]^{2-}$ and $[c\text{-}B_3(\mu_2\text{-}P)_3]^{2-}$ species are -46.1, -18.2 ppm and -38.9, -18.2, respectively. We also computed the NICS$_{zz}$-scan curve of diborane, B_2H_6, which showed all the characteristics of the NICS$_{zz}$-scan curves of pure σ-aromatics. It is a sharp symmetric curve with half-band width of 1.3 Å, with the NICS$_{zz}$(0) and NICS$_{zz}$(1) values being -20.8 and -6.1 ppm, respectively. On the basis of the linear relationship given in Figure 2 and using the R_{av} value of 0.717

Å, one obtains a NICS$_{zz}$(0) value of -20.4 ppm, which is in excellent agreement with the computed NICS$_{zz}$(0) value of -20.8 ppm.

In summary, all 2e- and 6e-σ-aromatics studied herein are characterized by sharp NICS$_{zz}$-scan curves symmetric around the z-axis (perpendicular to the ring plane) with the NICS$_{zz}$ values decaying rapidly and monotically with respect to *R*, and having a half-band with approximately less than 3 Å.

3.3.   The case of the [c-Li$_3$]$^+$ and cyclopropane 2e-σ-aromatics

For the [c-Li$_3$]$^+$ (D_{3h}) cation, another 2e-σ-aromatic prototype, the NICS$_{zz}$-scan curve, has also the features of the NICS$_{zz}$-scan curves of the pure σ-aromatic, but its half-band width is greater than 3 Å (3.7 Å). The broadening of the NICS$_{zz}$-scan curve of [c-Li$_3$]$^+$ σ-aromatic is probably due to the bigger size of the three-membered Li$_3$ ring (R_{av} = 1.704 Å) that renders weaker the overlap of the 2s orbitals forming the 3c-2e bond. This is also mirrored on the estimated interaction energy between the Li$_2$ and Li$^+$ fragments (-45.66 kcal/mol), which is much smaller than the interaction energy between the H$_2$ and H$^+$ fragments to form the [c-H$_3$]$^+$ species (-154.03 kcal/mol). Another plausible reason for the broadening of the NICS$_{zz}$-scan curve of [c-Li$_3$]$^+$ σ-aromatic might be the contribution of the intrinsic local circulation of electrons around the nuclei to the diatropic NICS values. The pure σ-aromaticity in the [c-Li$_3$]$^+$ cation was previously justified by Alexandrova and Boldyrev [63].

Considering the ring current model one would expect the $\sigma_{zz}^d / \sigma_{zz}^d$(max) *versus z* and the *NICS / NICS*$_{max}$ *versus z* curves to be similar:

$$\frac{\sigma_{zz}^d}{\sigma_{zz}^d(\text{max})} \approx \frac{NICS}{NICS_{max}}$$

According to quantum theory for the σ_{zz}^d(max) occurring in the molecular plane (z = 0) for the *NICS*$_{max}$ will have:

$$NICS_{max} = -\kappa \frac{e^2 \mu_0}{8\pi m_e} \frac{1}{R_{av}}$$

For two σ-aromatics exhibiting *s*-orbital aromaticity it can be easily written:

$$\frac{NICS_{max1}}{NICS_{max2}} = \frac{R_{av2}}{R_{av1}}$$

If we use as a reference σ-aromatic the prototype [c-H$_3$]$^+$ cation we obtain the following relationship:

$$NICS_{max2} = -\frac{17.05}{R_{av2}}$$

On the basis of the above relationship we predict for the [c-Li$_3$]$^+$ cation a NICS$_{max}$ value of -10.0 ppm very close to the estimated NICS$_{zz}$(0) value of -11.2 ppm.

Cyclopropane being a saturated system was also found to be a strongly σ-aromatic molecule. Cyclopropane exhibits a ring current density induced by a perpendicular external magnetic field arising in the σ framework that is intense, diatropic and annular. The hallmarks of the σ-ring current in cyclopropane is reflected on the shape of the NICS$_{zz}$-scan curve, which corresponds to a symmetric curve with a maximum at z = 0 and a half-band width around 3.2 Å. Moreover, the main feature of the

strong diatropic circulation in [c-C$_3$H$_6$], which reaches maximal intensity (j_{max} = 0.121 a.u.) outside the line of carbon centers [64,65], accounts well for the slight broadening of the NICS$_{zz}$-scan curve (half-band width > 3 Å). The calculation of the CMO-NICS$_{zz}$ values for cyclopropane in D_{3h} symmetry showed that the Walsh orbitals HOMO,-1 ($2e'$), being σ-type MOs, have positive NICS$_{zz}$ value of 22.2 ppm, the HOMO-2,-3 ($1e''$), being π-type MOs, have also positive NICS$_{zz}$ value of 8.1 ppm and therefore induce σ- and π-type paratropic ring currents, respectively. On the other hand, the HOMO-5 ($1a_2''$), a π-type MO, has negative NICS$_{zz}$ value of -8.7 ppm, which cancels the induced π-paratropic ring current from the $1e''$ MOs. The remaining HOMO-4 ($2a_1'$), HOMO-6,-7 ($1e'$) and HOMO-8 ($1a_1'$) all being σ-type MOs, have negative NICS$_{zz}$ values of -5.4, -18.8 and -21.3 ppm respectively. The CMO-NICS$_{zz}$ results are nicely mirrored on the shape of the NICS$_{zz}$-scan curve of cyclopropane. It is interesting to notice that Pelloni *et al.* [65] demonstrated that both the large negative NICS value and anisotropies of cyclopropane are mainly determined by the in-plane components rather than the more relevant out-of-plane contribution. The existence of σ-aromaticity in cyclopropane has recently been challenged by *ab initio* valence bond (VBSCF/cc-PVTZ) computations which revealed directly that the σ-aromatic stabilization energy of cyclopropane is, at most, 3.5 kcal/mol relative to propane [66]. However, such small energy difference raised the question whether the cyclopropane is really the σ-aromatic paradigm.

3.4.   The NICS$_{zz}$-scan curves of the M$_3$(μ_2-CO)$_3$(CO)$_3$ (M = Ni, Pd, Pt) molecules predict their σ-aromaticity

Let us now explore the efficiency of the NICS$_{zz}$-scan profiles to predict the pure σ-aromaticity characterizing the M$_3$(μ_2-CO)$_3$(CO)$_3$ (M = Ni, Pd, Pt) molecules. Recently, R. B. King [67] applied the σ-aromaticity model used for cyclopropane to Group 8 trinuclear metal-carbonyl complexes, [M$_3$(CO)$_{12}$] (M = Fe, Ru, Os). The σ-aromaticity of these molecules was further verified by a structural and NICS analysis reported recently [68]. According to this model the bonding in the M$_3$ triangles is composed by a core 3c-2e bond of Hückel topology formed by overlap of inward pointing radial hybrid orbitals of M and a surface (in-plane) 3c-4e bond of Möbius topology formed by tangential p-orbitals of M. Notice that for the M$_3$(μ_2-CO)$_3$(CO)$_3$ (M = Ni, Pd, Pt) molecules the presence of the μ_2-CO ligands precludes the 3c-4e Möbius surface bonding orbitals. The NICS$_{zz}$-scan curves of the Pt$_3$(μ_2-CO)$_3$(CO)$_3$ molecule along with the molecular orbital energy level diagram, symmetries, 3D molecular orbital pictures and lowest T$_{x,y}$-allowed transitions contributing to the diamagnetic ring current are visualized in Figure 3, while the most salient features of the NICS$_{zz}$-scan curves along with the half-band widths and R_{av} values of the rings of the M$_3$(μ_2-CO)$_3$(CO)$_3$ (M = Ni, Pd, Pt) molecules are compiled in Table 2.

It can be seen that the NICS$_{zz}$-scan curves of the M$_3$ (M = Ni, Pd, Pt) clusters are sharp symmetric curves with half-band width less than 2 Å, illustrating their pure σ-aromatic character. The broadening of the NICS$_{zz}$-scan curves of the M$_3$(μ_2-CO)$_3$(CO)$_3$ (M = Ni, Pd, Pt) molecules (half-band width of 2.7-4.6 Å), could be attributed to the contribution of the diatropic NICS values of the strongly σ-aromatic c-M$_2$C rings to the diatropic NICS values of the M$_3$ core rings.

Table 2. The NICS values (ppm) calculated at the ring center, NICS(0) and 1.0 Å above the ring center, NICS(1), the zz-component of the shielding tensor element, $NICS_{zz}(0)$ and $NICS_{zz}(1)$ along with the half-band width (Å) and R_{av} (Å) for the $M_3(\mu_2\text{-}CO)_3(CO)_3$ (M = Ni, Pd, Pt) molecules computed at the B3LYP/SDD(Pd,Pt)∪6-311+G(d,p) (C,O) levels.

Compound	NICS(0)	NICS(1)	$NICS_{zz}(0)$	$NICS_{zz}(1)$	Half-band width	R_{av}
$Ni_3(\mu_2\text{-}CO)_3(CO)_3$ (C_{3v})	-34.2[a]	-21.0	-53.9[a]	-36.6	2.7	1.427
$Pd_3(\mu_2\text{-}CO)_3(CO)_3$ (D_{3h})	-30.2	-14.0	-27.7	-23.6	4.6	1.602
$Pt_3(\mu_2\text{-}CO)_3(CO)_3$ (D_{3h})	-39.3	-19.3	-37.9	-34.4	4.6	1.602

Figure 3. $NICS_{zz}$-scan profiles ($NICS_{zz}$ in ppm, R in Å) of the [c-$Pt_3(\mu_2\text{-}CO)_3(CO)_3$] complex, along with the molecular orbital energy level diagram, symmetries, 3D molecular orbital pictures and lowest $T_{x,y}$- and R_z-allowed transitions computed at the B3LYP/SDD(Pt)∪6-311+G(d,p) (C,O) level (solid and dash arrows indicate $T_{x,y}$- and R_z-allowed transitions respectively).
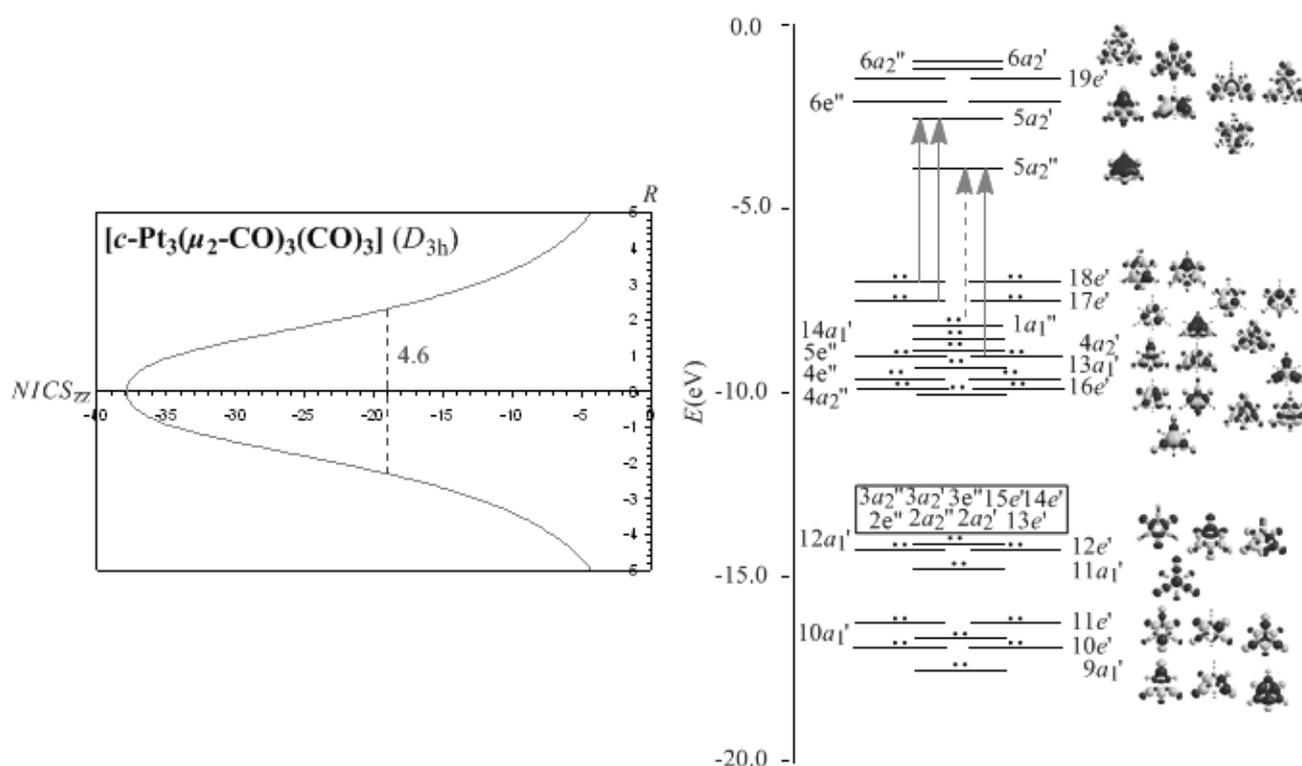
3.5. The $NICS_{zz}$-scan curves of triangular main group clusters exhibiting double ($\sigma + \pi$)-aromaticity

Let us further examine the $NICS_{zz}$-scan curves of three-membered rings of main group atoms, which have been extensively studied and characterized as double ($\sigma + \pi$)-aromatics. All these molecules showed $NICS_{zz}$-scan curves symmetric around the z-axis with the $NICS_{zz}$ values decaying monotonically with respect to R, but with half-band width greater than 3 Å. The $NICS_{zz}$-scan profiles in the form of $NICS_{zz}/NICS_{zz}^{max}$ *versus* R curves for selected triangular main group clusters exhibiting

double ($\sigma + \pi$)-aromaticity are given in Figure 4, while the most salient features of the NICS$_{zz}$-scan curves along with the R_{av} values of the rings are compiled in Table 3.

Figure 4. The NICS$_{zz}$-scan profiles in the form of NICS$_{zz}$/NICS$_{zz}$^{max} *versus R* (in Å) curves for selected triangular main group clusters exhibiting double ($\sigma + \pi$)-aromaticity.
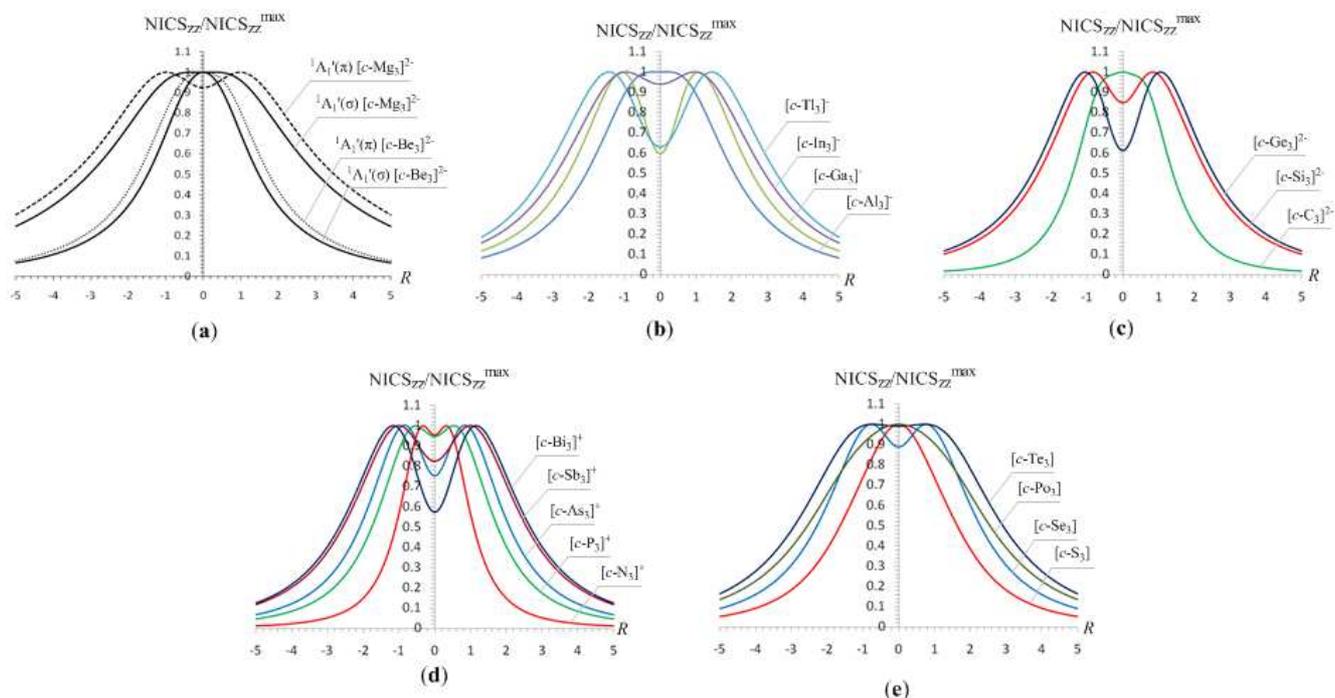
3.5.1. Magnetotropicity of [c-Be$_3$]$^{2-}$ and [c-Mg$_3$]$^{2-}$ clusters

The ^{1}A$_1'$(σ) ground-state occupation in D_{3h} symmetry of 8 valence electrons for the [c-Be$_3$]$^{2-}$ and [c-Mg$_3$]$^{2-}$ clusters was found to be HOMO-3 (a_1'), HOMO-1,2 (e'), HOMO (a_1'). The lowest T$_{x,y}$-allowed transitions are the HOMO (a_1') $\rightarrow$ LUMO+1,+2 (e') and HOMO (a_1') $\rightarrow$ LUMO+3,+4 (e') with excitation energies of 1.22 and 1.76 eV for [c-Be$_3$]$^{2-}$ cluster and 0.67 and 0.94 eV for [c-Mg$_3$]$^{2-}$ cluster respectively. In these transitions a σ-type (a_1') MO is involved in the excitation inducing a σ-diatropic ring current and therefore [c-Be$_3$]$^{2-}$ and [c-Mg$_3$]$^{2-}$ clusters in their ^{1}A$_1'$(σ) ground-states exhibit σ-aromaticity in line with the results concerning the tuning of aromaticity in trigonal alkaline earth metal clusters reported recently [69]. The NICS$_{zz}$-scan curves of the [c-Be$_3$]$^{2-}$ and [c-Mg$_3$]$^{2-}$ clusters in their ^{1}A$_1'$(σ) ground-states have the features of the NICS$_{zz}$-scan curves of pure σ-aromatics but their half-band width is greater than 3 Å (3.7 Å). The broadening of the NICS$_{zz}$-scan curves could be explained as in the case of the [c-Li$_3$]$^+$ σ-aromatic.

We have also investigated the aromaticity/antiaromaticity of the ^{1}A$_1'$(π) electronic states of the [c-Be$_3$]$^{2-}$ and [c-Mg$_3$]$^{2-}$ clusters found as local minima at 4.6 and 5.3 kcal/mol higher in energy than the ^{1}A$_1'$(σ) ground states at the B3LYP/6-311+G(d) level in line with the results reported by Matito *et al*. [68]. The ^{1}A$_1'$(π) electronic state occupation in D_{3h} symmetry of 8 valence electrons for the [c-Be$_3$]$^{2-}$ and [c-Mg$_3$]$^{2-}$ clusters was found to be HOMO-3 (a_1'), HOMO-1,2 (e'), HOMO (a_2''). It can be seen that the lowest T$_{x,y}$-allowed transitions are the HOMO-1,2 (e') $\rightarrow$ LUMO (a_1') and HOMO (a_2'') $\rightarrow$

LUMO+5,6 (e''). In the first transition a σ-type (a_1') MO is involved in the excitation inducing a σ-diatropic ring current, while in the second transition a π-type (a_2'') MO is involved inducing a π-diatropic ring current.

Table 3. The NICS values (in ppm) calculated at the ring center, NICS(0) and 1.0 Å above the ring center, NICS(1), the zz-component of the shielding tensor element, $NICS_{zz}(0)$ and $NICS_{zz}(1)$, the R_{max} (in Å) and the corresponding $NICS_{zz}^{max}$ along with the R_{av} (in Å) for selected triangular (D_{3h}) main group double ($\sigma + \pi$)-aromatic clusters computed at the B3LYP/6-311+G(d,p) level.

Cluster	NICS(0)	NICS(1)	$NICS_{zz}(0)$	$NICS_{zz}(1)$	R_{max} (Å)	$NICS_{zz}^{max}$	Δ_{NICS}[a]	R_{av} (Å)
$[c\text{-}Be_3]^{2-}$ [b]	33.6	1.7	-44.1	-30.9	0.0	-44.1	0.0	1.245
$[c\text{-}Be_3]^{2-}$ [c]	-65.0	-31.8	-42.8	-34.5	0.0	-42.8	0.0	1.200
$[c\text{-}Mg_3]^{2-}$ [b]	-2.8	-4.0	-12.7	-12.2	0.4	-12.7	0.0	1.948
$[c\text{-}Mg_3]^{2-}$ [c]	-36.5	-24.3	-13.6	-14.7	1.0	-14.7	1.1	1.859
$[c\text{-}Al_3]^{-}$	-35.6	-26.7	-34.4	-30.6	0.0	-34.4	0.0	1.465
$[c\text{-}Al_3]^{+}$	-26.4	-19.5	-30.4	-29.0	0.5	-31.1	0.7	1.486
$[c\text{-}Ga_3]^{-}$	-27.3	-22.6	-15.0	-25.1	1.1	-25.2	10.2	1.473
$[c\text{-}Ga_3]^{+}$	-14.4	-14.6	-11.8	-24.6	1.1	-24.8	13.0	1.529
$[c\text{-}In_3]^{-}$	-6.1	-10.6	-13.0	-13.8	1.0	-13.8	0.8	1.743
$[c\text{-}Tl_3]^{-}$	16.6	1.7	-5.4	-8.1	1.4	-8.6	3.2	1.824
$[c\text{-}C_3]^{2-}$	13.2	-10.2	-15.4	-11.6	0.0	-15.4	0.0	0.824
$[c\text{-}Si_3]^{2-}$	-3.1	-12.8	-26.4	-30.7	0.8	-31.0	4.6	1.355
$[c\text{-}Ge_3]^{2-}$	-4.2	-13.4	-21.2	-34.6	1.1	-34.6	13.4	1.444
$[c\text{-}N_3]^{+}$	-8.1	-20.5	-59.5	-35.3	0.3	-62.3	2.8	0.761
$[c\text{-}P_3]^{+}$	-12.9	-18.3	-40.3	-37.5	0.5	-42.6	2.3	1.221
$[c\text{-}As_3]^{+}$	-13.3	-18.4	-30.2	-39.4	0.8	-40.1	9.9	1.359
$[c\text{-}Sb_3]^{+}$	0.6	-7.3	-18.5	-22.4	1.0	-22.4	3.9	1.630
$[c\text{-}Bi_3]^{+}$	-11.8	-15.3	-19.2	-33.0	1.2	-33.4	14.2	1.686
$c\text{-}S_3$	-42.3	-7.0	-32.4	-23.9	0.0	-32.4	0.0	1.226
$c\text{-}Se_3$	-42.7	-9.8	-23.3	-25.6	0.8	-26.2	2.9	1.382
$c\text{-}Te_3$	-23.8	-7.5	-13.1	-13.1	0.8	-13.2	0.1	1.669
$c\text{-}Po_3$	-29.4	-9.5	-18.4	-16.7	0.0	-16.7	0.0	1.705

[a] $\Delta_{NICS} = NICS_{zz}^{max} - NICS_{zz}(0)$. [b] $^1A_1'(\sigma)$ ground state. [c] $^1A_1'(\pi)$ electronic state.

In the $[c\text{-}Be_3]^{2-}$ cluster the σ-diatropic ring current overwhelms the π-diatropic ring current because of the lower excitation energy (1.59 eV) of the first transition relative to the second one (1.67 eV). This observation accounts well for the broadening of the $NICS_{zz}$-scan curve of the $[c\text{-}Be_3]^{2-}$ cluster having its maximum at z = 0. On the other hand, in the $[c\text{-}Mg_3]^{2-}$ cluster the π-diatropic ring current is much stronger than the σ-diatropic ring current because of the much lower excitation energy (0.94 eV) of the π-type transition relative to the σ-type one (2.19 eV). It is obvious then why the $NICS_{zz}$-scan curve of the $^1A_1'(\pi)$ $[c\text{-}Mg_3]^{2-}$ exhibits two maxima at a certain distance above and below the molecular plane. Kuznetsov and Boldyrev showed that the unusual $[c\text{-}Mg_3]^{2-}$ trigonal planar cluster exhibits an

extraordinary type of aromaticity, where π-aromaticity occurs without initial formation of the σ-framework [70].

3.5.2. Magnetotropicity of the $[c\text{-}E_3]^-$ (E = Al, Ga, In, Tl), $[c\text{-}E_3]^{2-}$ (E = C, Si, Ge), $[c\text{-}E_3]^+$ (E = N, P, As, Sb, Bi) and $[c\text{-}E_3]$ (E = S, Se, Te, Po) rings

The $NICS_{zz}$-scan curves of the $[c\text{-}Al_3]^-$, $[c\text{-}Ga_3]^-$, $[c\text{-}In_3]^-$ and $[c\text{-}Tl_3]^-$ clusters looks like the mirror image of a typical scan of double ($\sigma + \pi$)-aromatic molecules (Figure 4b). The multiple aromaticity of the $[c\text{-}X_3]^-$ (X = Al, and Ga) clusters was recently verified by Boldyrev *et al.* [56,62] through a molecular orbital analysis, and by Dixon *et al.* [71] by estimating the resonance energy using high-level *ab initio* quantum chemical calculations. The estimated excitation energies of the lowest $T_{x,y}$- and R_z-allowed transitions of the three-membered rings of main group atoms are compiled in Table 4.

Table 4. Estimated excitation energies (in eV) of the lowest $T_{x,y}$- and R_z-allowed transitions of the three-membered rings of main group atoms.

Cluster	Excitations	
	$a_1' \rightarrow e'$ (σ-type)	$a_2'' \rightarrow e''$ (π-type)
$[c\text{-}Al_3]^-$	1.58	3.16
$[c\text{-}Ga_3]^-$	1.50	2.46
$[c\text{-}In_3]^-$	1.11	2.62
$[c\text{-}Tl_3]^-$	1.12	2.45
$[c\text{-}C_3]^{2-}$	5.18	7.39
$[c\text{-}Si_3]^{2-}$	3.41	3.61
$[c\text{-}Ge_3]^{2-}$	2.58	2.08
$[c\text{-}N_3]^+$	18.04	11.11
$[c\text{-}P_3]^+$	9.47	5.60
$[c\text{-}As_3]^+$	8.29	4.63
$[c\text{-}Sb_3]^+$	6.56	3.75
$[c\text{-}Bi_3]^+$	6.27	3.23
$[c\text{-}S_3]$	9.29	8.00
$[c\text{-}Se_3]$	7.98	7.29
$[c\text{-}Te_3]$	6.13	7.30[a]
$[c\text{-}Po_3]$	5.11	6.18[a]

[a] $e'' \rightarrow a_2''$ transition

The lowest $T_{x,y}$-allowed transitions of the three-membered rings of main group atoms are the $a_1' \rightarrow e'$ (σ-type) and $a_2'' \rightarrow e''$ (π-type) excitations. The coexistence of both the σ- and π-type transitions accounts well for the double ($\sigma + \pi$)-aromatic character of the aforementioned rings. The extent of contribution of the two types of transitions to the induced diatropic ring current is determined by the excitation energies of the σ- and (π-type) transitions (Table 4). Furthermore, removal of two electrons from the $[c\text{-}Al_3]^-$ and $[c\text{-}Ga_3]^-$ clusters affords $[c\text{-}Al_3]^+$ and $[c\text{-}Ga_3]^+$ respectively, where the lowest σ-type transition disappears and therefore the π-diatropic ring current exceeds the σ-type one, a fact

imprinted on the $NICS_{zz}$-scan curves of $[c\text{-}Al_3]^+$ and $[c\text{-}Ga_3]^+$ clusters which exhibit two maxima at a certain distance above and below the molecular plane (Table 3). The estimated excitation energies also illustrate that the induced π-diatropic ring current slightly overwhelms the σ-diatropic ring current in the $[c\text{-}N_3]^+$ and $[c\text{-}P_3]^+$ clusters, which unequivocally exhibit double $(\sigma + \pi)$-aromaticity. In effect, the $NICS_{zz}$-scan curves (Fig. 4d) for the $[c\text{-}N_3]^+$ and $[c\text{-}P_3]^+$ clusters are typical for double $(\sigma + \pi)$-aromatic molecules with slightly stronger π- than σ-aromatic character. According to the estimated excitation energies the $[c\text{-}As_3]^+$, $[c\text{-}Sb_3]^+$ and $[c\text{-}Bi_3]^+$ clusters are doubly $(\sigma + \pi)$-aromatic molecules with slightly higher π- than σ-aromatic character. Finally, the $NICS_{zz}$-scan curves of the 18 valence electron $[c\text{-}S_3]$, $[c\text{-}Se_3]$, $[c\text{-}Te_3]$ and $[c\text{-}Po_3]$ clusters are also typical for double $(\sigma + \pi)$-aromatics with varying magnitude of π- and σ-aromatic character (Fig. 4e). For $[c\text{-}S_3]$ and $[c\text{-}Se_3]$ the π-component should be slightly stronger than the σ-one, while the opposite is true for the $[c\text{-}Te_3]$ and $[c\text{-}Po_3]$ clusters. This is compatible with the excitation energies of the lowest $T_{x,y}$-allowed transitions for the neutral triangular chalcogen clusters (Table 4). Computed GIAO-SCF NICS and localized (LMO) NICS analysis of the A_n, (A = O, S, Se; n = 3-6) clusters carried out by Schleyer *et al.* [72] indicated that the σ-ring electrons are chiefly responsible for the zigzac NICS(0) behavior of the A_n rings with the A_3 clusters being aromatic. It is important to notice that the double $(\sigma + \pi)$-aromaticity of all three-membered rings of main group atoms studied is reflected on the excellent linear correlation of the $NICS_{zz}(0)$ values with the R_{av} values of the rings shown in Figure 5.

Figure 5. Linear relationship between $NICS_{zz}(0)$ (in ppm) and R_{av} (in Å) for triangular (D_{3h}) main group double $(\sigma + \pi)$-aromatic clusters.
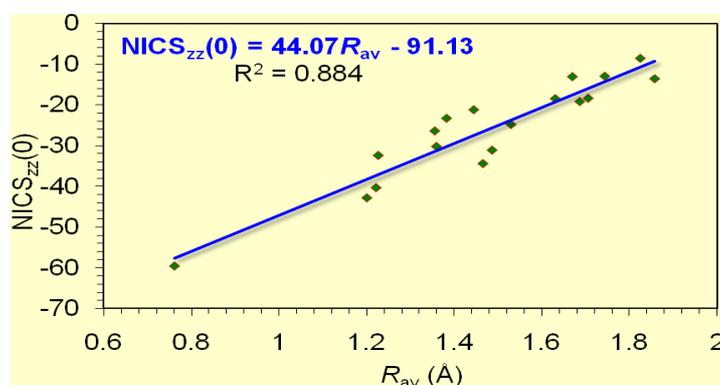
In summary all triangular main group clusters exhibiting double $(\sigma + \pi)$-aromaticity studied herein are characterized by broad $NICS_{zz}$-scan curves with half-band width >3 Å indicating double $(\sigma + \pi)$-aromaticity with comparable contribution to the induced total diatropic ring current from the σ- and π-diatropic ring currents.

3.6.   The $NICS_{zz}$-scan curves of four- and five-membered rings of main group atoms exhibiting double $(\sigma + \pi)$-aromaticity

Next we examined the $NICS_{zz}$-scan curves of four- and five -membered rings of main group atoms, which have been extensively studied and characterized as double $(\sigma + \pi)$-aromatics. The $NICS_{zz}$-scan profiles in the form of $NICS_{zz}/NICS_{zz}^{max}$ *versus* R curves of the $[c\text{-}B_4]^{2-}$, $[c\text{-}Al_4]^{2-}$, $[c\text{-}Ga_4]^{2-}$, $[c\text{-}In_4]^{2-}$,

$[c\text{-Tl}_4]^{2-}$, $[c\text{-Si}_4]^{2+}$ and $[c\text{-Mg}_4]^{2+}$ clusters given in Figure 6 are symmetric around the z-axis with maximum at z = 0 and half-band width (except $[c\text{-B}_4]^{2-}$) greater than 3 Å.

> **Figure 6.** The $NICS_{zz}$-scan profiles in the form of $NICS_{zz}/NICS_{zz}^{max}$ *versus R* (in Å) curves for selected four- and five-membered rings of main group atoms exhibiting double $(\sigma + \pi)$-aromaticity.

(a)   (b)
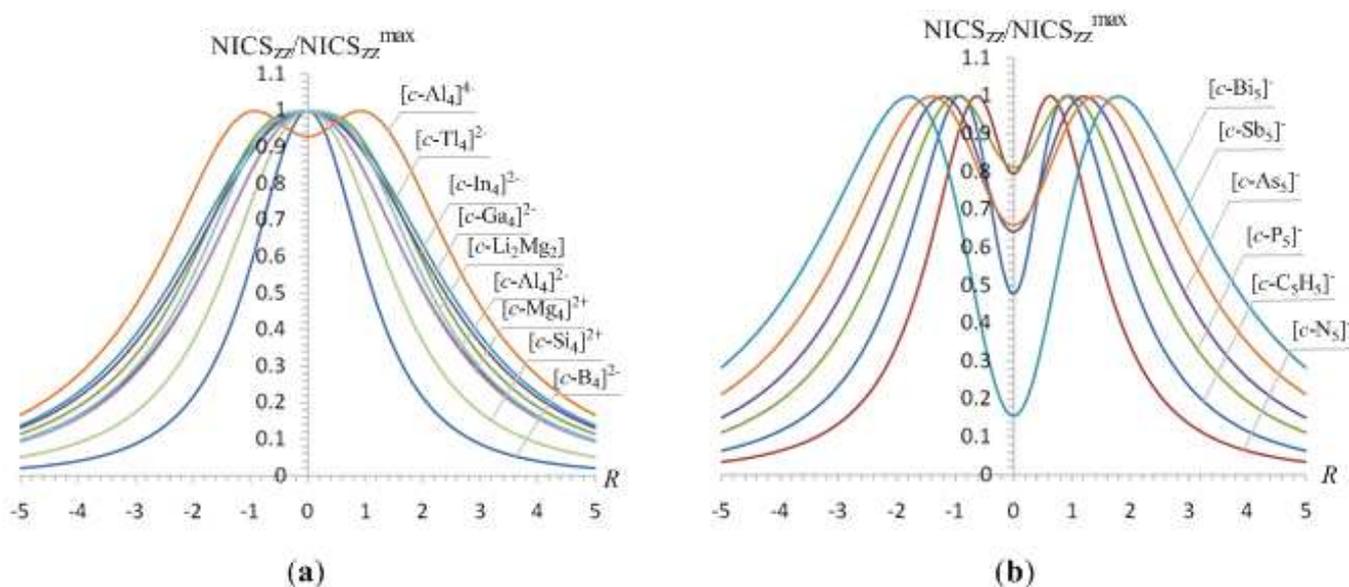
The $NICS_{zz}$-scan curves of the $[c\text{-Al}_4]^{4-}$ species as well as of the five-membered pnictogen $[c\text{-Pn}_5]^-$ (Pn = N, P, As, Sb, Bi) clusters exhibit two maxima at a certain distance above and below the molecular plane (Figure 6), which are typical for double $(\sigma + \pi)$-aromatics where the π-diatropic ring current overwhelms the σ-type one. The most salient features of the $NICS_{zz}$-scan curves of all these clusters along with the R_{av} values of the rings are compiled in Table 5.

> **Table 5.** The NICS values (ppm) calculated at the ring center, NICS(0) and 1.0 Å above the ring center, NICS(1), the zz-component of the shielding tensor element, $NICS_{zz}(0)$ and $NICS_{zz}(1)$, the R_{max} (in Å) and the corresponding $NICS_{zz}^{max}$ along with the R_{av} (in Å) for selected four- and five-membered σ-, π- and double $(\sigma + \pi)$-aromatic molecules.

Compound	NICS(0)	NICS(1)	$NICS_{zz}(0)$	$NICS_{zz}(1)$	R_{max} (Å)	$NICS_{zz}^{max}$	Δ_{NICS}[a]	R_{av}
$[c\text{-B}_4]^{2-}$ (D_{4h})	-44.8	-24.3	-83.4	-47.8	0.0	-83.4	0.0	0.727
$[c\text{-Al}_4]^{2-}$ (D_{4h})	-34.4	-27.7	-66.2	-54.9	0.0	-66.2	0.0	1.832
$[c\text{-Ga}_4]^{2-}$ (D_{4h})	-38.6	-29.7	-63.3	-57.6	0.0	-63.3	0.0	1.814
$[c\text{-In}_4]^{2-}$ (D_{4h})	-22.6	-20.9	-54.3	-47.9	0.0	-54.3	0.0	2.094
$[c\text{-Tl}_4]^{2-}$ (D_{4h})	-18.7	-18.7	-48.8	-43.8	0.0	-43.8	0.0	2.144
$[c\text{-Al}_4]^{4-}$ (D_{2h})	-6.0	-12.1	-30.0	-32.2	0.9	-32.3	2.3	1.885
$[c\text{-Si}_4]^{2+}$ (D_{4h})	-42.0	-28.8	-78.1	-58.0	0.0	-78.1	0.0	1.633

Table 5. *Cont.*

Compound	NICS(0)	NICS(1)	$NICS_{zz}(0)$	$NICS_{zz}(1)$	R_{max} (Å)	$NICS_{zz}^{max}$	Δ_{NICS}^{a}	R_{av}
$[c\text{-}Mg_4]^{2+}$ (D_{4h})	-10.7	-8.6	-31.0	-25.7	0.0	-31.0	0.0	2.213
$c\text{-}Li_2Mg_2$ (D_{2h})	4.0	-1.0	-26.6	-23.6	0.0	-26.6	0.0	2.066
$[C_5H_5]^-$ (D_{5h})	-12.6	-9.6	-16.2	-33.7	0.9	-34.0	17.8	1.204
$[c\text{-}N_5]^-$ (D_{5h})	-16.5	-16.5	-41.2	-45.2	0.6	-51.9	10.7	1.128
$[c\text{-}P_5]^-$ (D_{5h})	-16.7	-15.8	-31.8	-39.3	1.0	-39.3	7.5	1.808
$[c\text{-}As_5]^-$ (D_{5h})	-15.3	-14.7	-22.3	-33.9	1.2	-34.6	12.3	1.993
$[c\text{-}Sb_5]^-$ (D_{5h})	-9.0	-9.5	-14.9	-21.2	1.4	-22.5	7.6	2.347
$[c\text{-}Bi_5]^-$ (D_{5h})	-9.3	-9.5	-3.2	-15.2	1.8	-20.8	17.7	2.464

[a] $\Delta_{NICS} = NICS_{zz}^{max} - NICS_{zz}(0)$

3.6.1. Magnetotropicity of the $[c\text{-}E_4]^{2-}$ (E = B, Al, Ga, In, Tl), $[c\text{-}Si_4]^{2+}$, $[c\text{-}Mg_4]^{2+}$, $[c\text{-}Li_2Mg_2]$, $[c\text{-}C_5H_5]^-$, and $[c\text{-}E_5]^-$ (E = N, P, As, Sb, Bi) rings

Let us now analyze the shapes of the $NICS_{zz}$-scan curves of the four- and five-membered rings of main group atoms in relation with the relative ratio of the induced σ- and π-diatropic ring currents. The ground-state ($^1A_{1g}$) occupation in D_{4h} symmetry of 14 valence electrons for the $[c\text{-}Al_4]^{2-}$, $[c\text{-}Ga_4]^{2-}$, $[c\text{-}In_4]^{2-}$ and $[c\text{-}Tl_4]^{2-}$ clusters was found to be $1a_{1g}^2 1e_u^4 1b_{1g}^2 1b_{2g}^2 2a_{1g}^2 1a_{2u}^2$. In $[c\text{-}In_4]^{2-}$ cluster there is an inversion of the $1a_{2u}$ and $2a_{1g}$. For the $[c\text{-}B_4]^{2-}$ cluster the electron occupation follows a different order, e.g. $1a_{1g}^2 1e_u^4 1a_{2u}^2 1b_{2g}^2 2a_{1g}^2 1b_{1g}^2$. The computed excitation energies of the main translational transitions of $[c\text{-}Al_4]^{2-}$, $[c\text{-}Ga_4]^{2-}$, $[c\text{-}In_4]^{2-}$, $[c\text{-}Tl_4]^{2-}$ and $[c\text{-}Si_4]^{2+}$ clusters are given in Table 6.

Table 6. Estimated excitation energies (in eV) of the main translational σ- and π-type transitions of double ($\sigma + \pi$)-aromatic four-membered $[c\text{-}Al_4]^{2-}$, $[c\text{-}Ga_4]^{2-}$, $[c\text{-}In_4]^{2-}$, $[c\text{-}Tl_4]^{2-}$ and $[c\text{-}Si_4]^{2+}$ clusters in D_{4h} symmetry.

excitation	type	Excitation energy				
		$[c\text{-}Al_4]^{2-}$	$[c\text{-}Ga_4]^{2-}$	$[c\text{-}In_4]^{2-}$	$[c\text{-}Tl_4]^{2-}$	$[c\text{-}Si_4]^{2+}$
$a_{1g} \rightarrow e_u$	σ-	2.00	0.56	1.92	1.96	3.14
$a_{2u} \rightarrow e_g$	**π-**	**2.30**	**1.17**	**2.07**	**2.03**	**3.68**
$b_{2g} \rightarrow e_u$	σ-					4.20
$b_{1g} \rightarrow e_u$	σ-					4.85

Based on the estimated excitation energies of the lowest $T_{x,y}$- allowed σ- and π-type $3a_g \rightarrow 3e_u$ (1.42 eV) and $1a_{2u} \rightarrow 1e_g$ (4.74 eV) transitions compiled in Table 6 we predict that the $[c\text{-}B_4]^{2-}$ posses rather pure σ-aromatic character, which is also mirrored on the shape of the symmetric sharp (half-band width = 2.3 Å) $NICS_{zz}$-scan curve (Figure 6a). The same holds true for the $[c\text{-}Mg_4]^{2+}$ and $[c\text{-}Li_2Mg_2]$ clusters where the occupation of 6 valence electrons was found to be $1e_u^4 1a_{1g}^2$ for $[c\text{-}Mg_4]^{2+}$ (D_{4h}) and $1a_g^2 1b_{1u}^2 1b_{2u}^2$ for $[c\text{-}Li_2Mg_2]$ (D_{2h}). The estimated excitation energies of the lowest $T_{x,y}$-allowed transitions found to be 1.12 eV for the σ-type $e_u \rightarrow a_{1g}$ in $[c\text{-}Mg_4]^{2+}$ (D_{4h}) and 2.06 eV for the σ-type $b_{2u} \rightarrow a_{1g}$ and 4.92 eV for the π-type $a_g \rightarrow b_{3u}$ in $[c\text{-}Li_2Mg_2]$ (D_{2h}) accounts well for the shape of the

NICS$_{zz}$-scan curves (Fig. 6a). As in the case of the [c-Li$_3$]$^+$ (D_{3h}) cation the broadening of the NICS$_{zz}$-scan curves of [c-Mg$_4$]$^{2+}$ and [c-Li$_2$Mg$_2$] clusters is probably due to the bigger size of the four-membered rings (R_{av} = 2.213 and 2.066 Å in c-Mg$_4$]$^{2+}$ and [c-Li$_2$Mg$_2$] rings respectively) and/or to the contribution of the intrinsic local circulation of electrons around the nuclei to the diatropic NICS values. The pure σ-aromaticity in the [c-Mg$_4$]$^{2+}$ and [c-Li$_2$Mg$_2$] clusters was previously justified by Alexandrova and Boldyrev [57]. In all these double ($\sigma + \pi$)-aromatic clusters the σ-aromatic character overwhelms the π-aromatic one enforcing the broadening of the NICS$_{zz}$-scan curves, which have half-band widths greater than 4 Å (Fig. 6). Of particular importance is the excellent linear correlation of the NICS$_{zz}$(0) values of the four-membered rings of 13 group atoms with the R_{av} values of the rings (Figure 7).

Figure 7. Linear relationship between NICS$_{zz}$(0) (in ppm) and R_{av} (in Å) for the four-membered rings of 13 group atoms.
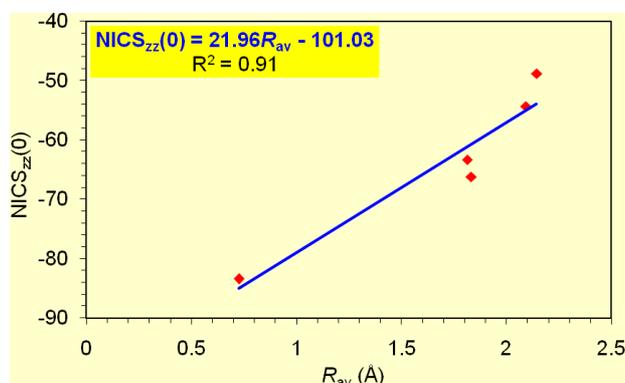
The double ($\sigma + \pi$)-aromaticity of the [c-Al$_4$]$^{2-}$ cluster was first introduced in a seminal work published in *Science* by Boldyrev *et al*. [73] and subsequently justified by the use of different criteria of aromaticity, such as the induced magnetic field analysis [74], the aromatic ring current shielding (ARCS) [39,75], the ring current maps [76-79], NICS [80], resonance energy (RE) estimations [39,81], valence bond (VB) calculations [82], bifurcation analysis of electron localization function (ELF) [83], conceptual DFT descriptors [84], and quantum theory of atoms in molecules (QTAIM) calculations [85]. It should also be noticed that Sundholm *et al*. [75] based on ARCS calculations on the [c-Al$_4$]$^{2-}$, [c-Ga$_4$]$^{2-}$, [c-In$_4$]$^{2-}$ and [c-Tl$_4$]$^{2-}$ indicated that all these species are aromatic, the calculated ring-current susceptibilities and the (ring radius) found to be 16.2 nA/T (194 pm), 17.2 nA/T (190 pm), 19.3 nA/T (210 pm) and 18.4 nA/T (241 pm) respectively, at the 3-VE+sp2df HF level.

The NICS$_{zz}$-scan curve of the [c-Al$_4$]$^{4-}$ cluster exhibits two maxima at a distance of 0.9 Å above and below the molecular plane (Fig. 6a), which is typical for double ($\sigma + \pi$)-aromatics where the π-type diatropic ring current exceeds slightly the σ-type one. In effect, this is compatible with the estimated excitation energies of the T$_{x,y}$-allowed σ-type $a_g \rightarrow b_{2u}$ (1.27 eV) and π-type $b_{3u} \rightarrow a_g$ (1.58 eV) and $a_g \rightarrow b_{3u}$ (2.05 eV) transitions. Notice the contribution of two T$_{x,y}$-allowed π-transitions to the π-diatropic ring current in [c-Al$_4$]$^{4-}$ cluster.

The NICS$_{zz}$-scan curve of the [c-Si$_4$]$^{2+}$ cluster, which is isoelectronic to [c-Al$_4$]$^{2-}$ one, is typical for double ($\sigma + \pi$)-aromatics where the σ-type diatropic ring current overwhelms remarkably the π-type one. The curve is symmetric around the z-axis with a half-band width of 3.1 Å (Figure 6a). The

stronger σ- than the π-aromatic character in $[c\text{-}Si_4]^{2+}$ cluster is reflected on the estimated excitation energies (Table 6) for the $a_{1g} \rightarrow e_u$, $b_{2g} \rightarrow e_u$, $b_{1g} \rightarrow e_u$ σ-type transitions, compared to the $a_{2u} \rightarrow e_g$ π-type transition. The $[c\text{-}Si_4]^{2+}$ has previously been characterized as triply aromatic, the triple aromaticity coming from the $\pi_{p\text{-}z}$-, $\sigma_{p\text{-}r}$- and $\sigma_{p\text{-}t}$-MOs (p-z, p-r and p-t are the vertical, radial and tangential $3p$ AOs of the Si atoms in the ring).

Finally, the NICS_{zz}-scan curves of the 26 valence electron five-membered pnictogen $[c\text{-}Pn_5]^-$ (Pn = N, P, As, Sb, Bi) clusters in D_{5h} symmetry are typical for double $(\sigma + \pi)$-aromatics with the π-aromatic character exceeding at a different extent the σ-aromatic character (Figure 6b). There is an increase of the π-aromatic character as one goes down in the 15 group pnictogen atom five-membered rings. The NICS_{zz}-scan curve of the five-membered cyclopentadienyl $[c\text{-}C_5H_5]^-$ ligand, a prototype of π-aromatic organic molecule, is also shown in Figure 6b.

The estimated excitation energies of the lowest $T_{x,y}$-allowed σ- and π-type transitions of the five-membered pnictogen $[c\text{-}Pn_5]^-$ (Pn = N, P, As, Sb, Bi) rings in D_{5h} symmetry tabulated in Table 7 account well for the shape of the NICS_{zz}-scan curves, which are characteristic for the double $(\sigma + \pi)$-aromaticity of the rings.

Table 7. Estimated excitation energies (in eV) of the main $T_{x,y}$-allowed σ- and π-type transitions of double $(\sigma + \pi)$-aromatic five-membered pnictogen $[c\text{-}Pn_5]^-$ (Pn = N, P, As, Sb, Bi) rings and the $[c\text{-}C_5H_5]^-$ ligand in D_{5h} symmetry.

excitation	Type	Excitation energy					
		$[c\text{-}N_5]^-$	$[c\text{-}P_5]^-$	$[c\text{-}As_5]^-$	$[c\text{-}Sb_5]^-$	$[c\text{-}Bi_5]^-$	$[c\text{-}C_5H_5]^-$
$e_1' \rightarrow a_1'$	σ-	9.24					
$e_1' \rightarrow e_2'$	σ-	9.82					
$e_2' \rightarrow e_2'$	σ-	9.84					
$e_1'' \rightarrow e_2''$	**π-**	**8.20**					
$e_1' \rightarrow a_1'$	σ-		5.86				
$e_1' \rightarrow e_2'$	σ-		5.99				
$e_1'' \rightarrow e_2''$	**π-**		**4.28**	**3.58**	**2.95**	**2.05**	
$e_1' \rightarrow a_1'$	σ-			5.23		4.72	
$e_1' \rightarrow e_2'$	σ-			5.10	5.10	3.84	
$a_1' \rightarrow e_1'$	σ-				5.996	4.99	
$e_1'' \rightarrow e_2''$	**π-**						6.31
$e_1' \rightarrow a_1'$	σ-						8.88
$e_2' \rightarrow e_1'$	σ-						8.59

It can be seen that all five-membered pnictogen $[c\text{-}Pn_5]^-$ (Pn = N, P, As, Sb, Bi) rings are double $(\sigma + \pi)$-aromatic with stronger π- than σ-aromatic character. The relative strength of the π- and σ-aromatic character of the rings can be expressed qualitatively by the ratio of the excitation energies of the π- and σ-type $T_{x,y}$-allowed transitions which were found to be 1.13, 1.37, 1.42, 1.73 and 1.88 for the $[c\text{-}N_5]^-$, $[c\text{-}P_5]^-$, $[c\text{-}As_5]^-$, $[c\text{-}Sb_5]^-$ and $[c\text{-}Bi_5]^-$ respectively. It is interesting to notice that for the series of the five-membered pnictogen $[c\text{-}Pn_5]^-$ clusters the $\text{NICS}_{zz}(0)$ values are linearly correlated

with the R_{av} values of the rings (Figure 8) following a similar pattern with that established for other series of aromatic clusters discussed herein.

The double $(\sigma + \pi)$-aromaticity of the pentagonal structures (D_{5h} symmetry) of the [c-Pn$_5$]$^-$ clusters was justified by Boldyrev *et al*. [86] using molecular orbital and photoelectron spectra analysis and compared with the aromaticity of the isovalent cyclopentadiene, [c-C$_5$H$_5$]$^-$ ligand. More recently, De Proft *et al*. [87] calculated the maps for the current density of the [c-P$_5$]$^-$ and [c-As$_5$]$^-$ clusters, which showed an apparently classic example of a diatropic ring current, but not solely π current. The current density at z = 1.0a$_0$ has approximately equal contribution from the four electrons in the $2e_1''$ HOMO (π-MO) and the four electrons in the $6e_2'$ HOMO-2 (σ-MO). The pattern of the current maps and orbital contributions of the [c-P$_5$]$^-$ and [c-As$_5$]$^-$ clusters are compatible with the NICS$_{zz}$-scan profiles.

Figure 8. Linear relationship between NICS$_{zz}$(0) (in ppm) and R_{av} (in Å) for the five-membered rings of 15 group atoms.
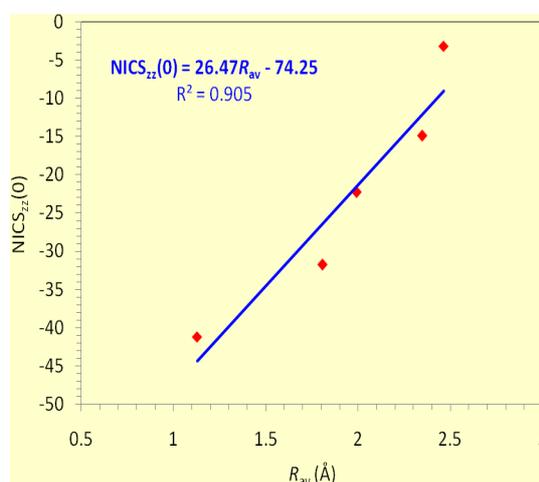
In summary the four- and five-membered rings of main group clusters exhibiting double $(\sigma + \pi)$-aromaticity studied herein are characterized, as in the case of the three-membered rings, by broad NICS$_{zz}$-scan curves with half-band width approximately > 3 Å indicating double $(\sigma + \pi)$-aromaticity with comparable contribution to the induced total diatropic ring current from the σ- and π-diatropic ring currents.

3.7.   *The NICS$_{zz}$-scan curves versus the orbital-type of aromaticity in organic molecules*

We next tested the predictive power of the NICS$_{zz}$-scan curves of the orbital-type of aromaticity for selected organic double $(\sigma + \pi)$- and pure π-aromatic molecules computed at the B3LYP/6-311+G(d,p) level. The NICS$_{zz}$-scan profiles in the form of NICS$_{zz}$/NICS$_{zz}$^{max} *versus R* curves of the selected organic molecules are depicted schematically in Figure 9, while the main features of the NICS$_{zz}$-scan curves of all molecules along with the R_{av} values of the rings are compiled in Table 8. The estimated excitation energies of the lowest T$_{x,y}$-allowed σ- and π-type transitions of the selected aromatic organic molecules are compiled in Tables 9-11.

Figure 9. The NICS$_{zz}$-scan profiles in the form of NICS$_{zz}$/NICS$_{zz}$^{max} *versus R* curves for selected aromatic organic molecules computed at the B3LYP/6-311+G(d,p) level.
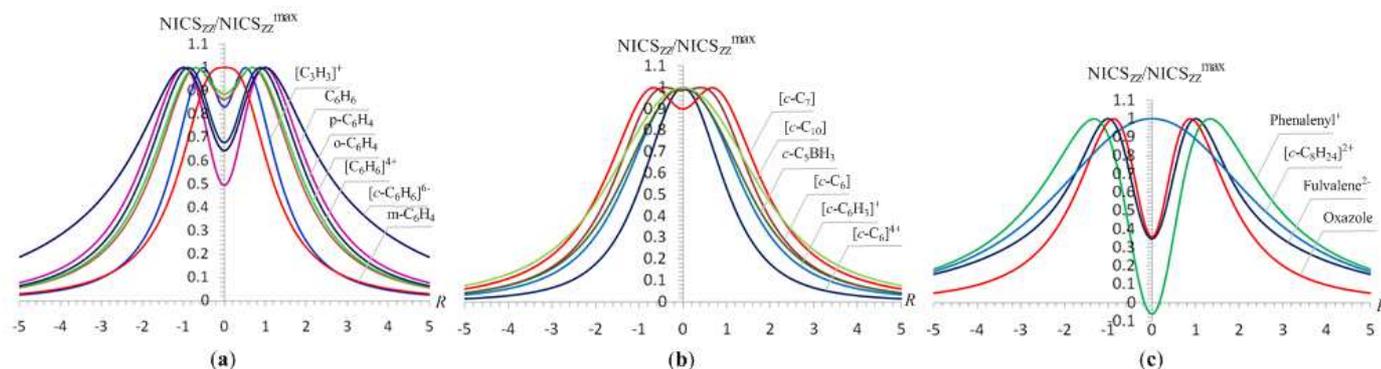
Table 8. The NICS values (in ppm) calculated at the ring center, NICS(0) and 1.0 Å above the ring center, NICS(1), the zz-component of the shielding tensor element, NICS$_{zz}$(0) and NICS$_{zz}$(1), the R_{max} (in Å) and the corresponding NICS$_{zz}$^{max} (ppm) along with R_{av} (Å) for selected aromatic organic molecules computed at the B3LYP/6-311+G(d,p) level.

Compound	NICS(0)	NICS(1)	NICS$_{zz}$(0)	NICS$_{zz}$(1)	R_{max}	NICS$_{zz}$^{max}	Δ_{NICS}[a]	R_{av}
$C_3H_3^+$ (D_{3h})	-22.9	-14.7	-31.1	-28.8	0.5	-37.4	6.3	0.787
C_6H_6 (D_{6h})	-8.0	-10.2	-14.5	-29.2	1.0	-29.2	14.7	1.395
$C_6H_6^{4-}$ (D_{6h})	-12.9	-14.1	-22.6	-37.9	1.0	-37.9	15.3	1.404
$C_6H_6^{6-}$ (D_{6h})	-16.0	-16.9	-26.7	-41.5	1.0	-41.5	14.8	1.395
o-C_6H_4 (C_{2v}) (S_0)	-18.0	-12.7	-30.7	-32.9	0.7	-34.7	4.0	1.369
m-C_6H_4 (C_{2v}) (S_0)	-42.2	-16.3	-64.4	-39.9	0.0	-64.4	0.0	1.225
p-C_6H_4 (D_{2h}) (S_0)	-29.5	-18.7	-63.6	-47.3	0.0	-63.6	0.0	1.388
C_6 (D_{3h})	-24.8	-12.0	-32.4	-28.3	0.4	-32.8	0.4	1.284
C_6^{4+} (D_{3h})	-61.4	-18.5	-69.0	-36.7	0.0	-69.0	0.0	1.356
$C_6H_3^+$ (D_{6h})	-42.7	-19.9	-72.4	-51.9	0.0	-72.4	0.0	1.313
C_5BH_3 (C_{2v})	-34.5	-16.8	-58.3	-43.2	0.0	-58.3	0.0	1.336
Fulvalene^{2-} (D_2)	-12.1	-16.6	-9.9	-28.5	1.0	-28.5	18.6	1.224
Phenalenyl$^+$ (D_{3h})	-3.6	-7.2	1.1	-17.3	1.3	-19.0	20.1	1.409
Oxazole (C_s)	-11.4	-9.7	-10.2	-27.9	0.9	-28.3	18.1	1.150
c-C_7 (C_{2v})	-16.9	-14.2	-32.3	-33.7	0.7	-35.9	3.6	1.483
c-$C_8H_{24}^{2+}$ (D_{4h})	-16.1	-13.7	-43.8	-39.0	0.0	-43.8	0.0	3.072
c-C_{10} (D_{5h})	-29.9	-22.3	-73.0	-59.0	0.0	-73.0	0.0	2.064

[a] Δ_{NICS} = NICS$_{zz}$^{max} - NICS$_{zz}$(0)

3.7.1. The $NICS_{zz}$-scan curves and magnetotropicity of the $[C_3H_3]^+$, C_6H_6, $[C_6H_6]^{4-}$, $[C_6H_6]^{6-}$, o-C_6H_4, m-C_6H_4, and p-C_6H_4 molecules

For the $[C_3H_3]^+$, C_6H_6, $[C_6H_6]^{4-}$, $[C_6H_6]^{6-}$, o-C_6H_4 (o-benzyne), m-C_6H_4 (m-benzyne), and p-C_6H_4 (p-benzyne) molecules the estimated excitation energies of the lowest $T_{x,y}$- and R_z-allowed σ- and π-type transitions are indicative of their double ($\sigma + \pi$)-aromatic character with varying σ-/π- ratio.

For the $[C_3H_3]^+$, C_6H_6, $[C_6H_6]^{4-}$ and $[C_6H_6]^{6-}$ molecules the contribution to the ring current from π-delocalized electrons is significantly higher than from σ-delocalized electrons (compare the excitation energies of the σ- and π-type transitions given in Table 9), a fact that is clearly reflected on the shape of the $NICS_{zz}$-scan curves (Figure 9a). It is important to notice that the occupation of the antibonding MOs of benzene with four and six electrons affording the anionic $[C_6H_6]^{4-}$ and $[C_6H_6]^{6-}$ species, which correspond to local minima in the PES, increase the aromaticity with respect to benzene molecule, despite the bonding from the bonding MOs will be offset by the effect of the occupied antibonding counterparts. This observation illustrates that the dynamic magnetic response of the aromatic species expressed by the NICS values could not be outweighed from the occupation of the antibonding MOs, since the induced ring current from the occupied bonding MOs could not be equal and of opposite sign with that from the occupied antibonding counterparts. However, the anionic $[C_6H_6]^{4-}$ and $[C_6H_6]^{6-}$ species should be unstable with respect to electron autodetachment in the gas phase and the results for these metastable species should be approached with caution as it is the case of the "all-metal aromatic" $[c\text{-}Al_4]^{2-}$ dianions [88].

For the singlet o- and m-benzyne isomers and the open-shell singlet p-benzyne the contribution to the ring current from π-delocalized electrons is also higher than from σ-delocalized electrons (compare the excitation energies of the σ- and π-type transitions given in Table 9). However, in the three isomers the induced paratropic current from π-delocalized electrons via the R_z-allowed transitions diminishes the induced π-diatropic ring current, thus rendering the contribution to the induced ring current from σ-delocalized electrons higher than from π-delocalized electrons, which is clearly reflected on the shape of the $NICS_{zz}$-scan curves (Figure 9a). It should be noticed that the relative aromaticities of the singlet o- and m-benzyne isomers and the open-shell singlet p-benzyne have previously been probed with a diverse aromaticity indicators [89]. Unlike benzene, the most negative NICS value occurs in the ring planes of the benzynes, which might indicate that the largest diamagnetic ring current is in the molecular plane. In effect, this is mirrored on the shapes of the $NICS_{zz}$-scan curves reported herein, which once again correctly predict the orbital-type of aromaticity in the isomeric benzyne molecules.

Table 9. Estimated excitation energies (in eV) of the main $T_{x,y}$- and R_z-allowed σ- and π-type transitions of selected aromatic organic molecules.

excitation	type	Excitation energies						
		$C_3H_3^+$	C_6H_6	$C_6H_6^{4-}$	$C_6H_6^{6-}$	o-C_6H_4	m-C_6H_4	p-C_6H_4
$a_2'' \to e''$	$\boldsymbol{\pi}$-	**10.03**						
$e' \to a_1'$	σ-	13.50						
$e' \to a_1'$	σ-	13.79						
$e_{1g} \to e_{2u}$	$\boldsymbol{\pi}$-		**6.59**	**6.32**				
$e_{1g} \to e_{2u}$	$\boldsymbol{\pi}$-		**8.78**	**7.07**				
$e_{2g} \to e_{2g}$	σ-		10.78	7.82	6.66			
$a_{1g} \to e_{1u}$	$\boldsymbol{\pi}$-				**2.80**			
$e_{1u} \to a_{1g}$	$\boldsymbol{\pi}$-				**3.93**			
$a_2 \to b_2$	$\boldsymbol{\pi}$-					**5.12**		
$a_1 \to b_2$	$\boldsymbol{\pi}$-					**5.15**		
$b_2 \to b_2$	σ-					8.71		
$a_1 \to a_2$	$\boldsymbol{\pi}$-$\mathbf{R_z}$					7.35		
$b_1 \to b_2$	$\boldsymbol{\pi}$-$\mathbf{R_z}$					5.11		
$a_2 \to b_1$	$\boldsymbol{\pi}$-						**5.41**	
$a_1 \to b_1$	σ-						5.65	
$a_1 \to b_2$	σ-						7.37	
$a_1 \to a_2$	$\boldsymbol{\pi}$-$\mathbf{R_z}$						6.75	
$b_1 \to b_2$	$\boldsymbol{\pi}$-$\mathbf{R_z}$						8.46	
$b_{2g} \to a_u$	$\boldsymbol{\pi}$-							**6.29**
$b_{3u} \to a_g$	$\boldsymbol{\pi}$-							**6.93**
$b_{2u} \to a_g$	σ-							8.00
$b_{1g} \to a_g$	$\boldsymbol{\pi}$-$\mathbf{R_z}$							**3.64**
$b_{1u} \to a_u$	$\boldsymbol{\pi}$-$\mathbf{R_z}$							**4.76**

3.7.2. The $NICS_{zz}$-scan curves and magnetotropicity of the c-C_6, [c-C_6]$^{4+}$, [c-C_6H_3]$^+$, c-C_5BH_3, c-C_7 and c-C_{10} molecules

The double ($\sigma + \pi$)-aromaticity is also present in the c-C_6, [c-C_6]$^{4+}$, [c-C_6H_3]$^+$, c-C_5BH_3, c-C_7 and c-C_{10} molecules. The double ($\sigma + \pi$)-aromaticity of the c-C_6 cluster was first discussed by Schleyer *et al.* [16]. It was claimed that the c-C_6 cluster is also σ-antiaromatic due to cyclic delocalization of its four lone-pair electrons. In effect, the estimated excitation energies of the lowest $T_{x,y}$- and R_z-allowed transitions in the c-C_6 cluster (Table 10) indicate a strong induced σ-diatropic ring current, which is partly outweighed from the induced σ-paratropic ring current due to the σ-R_z transition but still the induced σ-diatropic ring current seems to be stronger than the π-diatropic ring current, which is compatible with the shape of the $NICS_{zz}$-scan curve (Figure 9b). The estimated excitation energies of the lowest $T_{x,y}$-allowed transitions in the cationic [c-C_6]$^{4+}$ species clearly indicate that it is double ($\sigma + \pi$)-aromatic with σ-aromatic character much stronger than the π-aromatic one in line with the shape of the $NICS_{zz}$-scan curve (Figure 9b) having a half-band width of 2.1 Å, which is typical for completely σ-aromatic molecules.

Table 10. Estimated excitation energies (in eV) of the lowest $T_{x,y}$- and R_z-allowed σ- and π-type transitions of selected aromatic organic molecules.

excitation	type	Excitation energies					
		c-C_6	$[c$-$C_6]^{4+}$	$[c$-$C_6H_3]^+$	c-C_5BH_3	c-C_7	c-C_{10}
$e' \rightarrow a_1'$	σ-	3.96					
$e'' \rightarrow a_2''$	π-	**9.89**					
$a_1' \rightarrow a_2'$	σ-R_z	**9.14**					
$a_{1g} \rightarrow e_{1u}$	σ-		4.66				
$e_{1g} \rightarrow e_{2u}$	π-		**7.60**				
$a_1' \rightarrow e'$	σ-			6.51			
$e'' \rightarrow a_2''$	π-			**10.59**			
$a_1 \rightarrow b_2$	σ-				5.99		
$b_1 \rightarrow a_1$	π-				**6.55**		
$b_1 \rightarrow b_2$	π-R_z				**5.98**		
$a_1 \rightarrow b_2$	σ-					3.40	
$a_1 \rightarrow b_1$	π-					3.03	
$a_1 \rightarrow a_2$	σ-R_z					**6.36**	
$e_2' \rightarrow e_1'$	σ-						6.53
$e_1' \rightarrow e_2'$	σ-						8.35
$e_1'' \rightarrow e_2''$	π-						**8.57**

The $NICS_{zz}$-scan curves of the $[c$-$C_6H_3]^+$ and c-C_5BH_3 have the shape of the typical curves for double ($\sigma + \pi$)-aromatic molecules with σ-aromatic character much stronger than the π-aromatic one. Actually, the estimated excitation energies of the $[c$-$C_6H_3]^+$ and c-C_5BH_3 molecules (Table 10) are indicative of the much stronger σ- than π-aromatic character. For the c-C_5BH_3 molecule the contribution to the diatropic ring current from π-delocalized electrons is further decreased from the induced paratropic ring current due to the π-R_z transition. Hofmann and Berndt [90] showed that the the NICS(1) values of the double aromatic isoelectronic $[c$-$C_6H_3]^+$ and c-C_5BH_3 molecules are significantly larger than that of the benzene molecule due to the contribution of an additional aromatic system, namely the σ-aromatic component.

Akin to c-C_6 (D_{3h}) the c-C_{10} (D_{5h}) cluster was also proved to be a double ($\sigma + \pi$)-aromatic molecule with enhanced aromaticity due to an additional diatropic subsystem (the diatropic in-plane radial system) [16]. This is consistent with the estimated excitation energies of the σ- and π-type transitions (Table 10), which indicate that the σ-aromatic component should be larger than the π-aromatic one and is mirrored on the shape of the $NICS_{zz}$-scan curve shown in Figure 9b. Schleyer *et al*. [16] showed that the c-C_7 (C_{2v}) cluster has mixed aromatic (π) and antiaromatic (radial) systems. According to our calculations for the c-C_7 (C_{2v}) cluster the lowest σ- and π-$T_{x,y}$-allowed transitions have much lower excitation energies than the σ-R_z-allowed ones (Table 10) and therefore it is expected to be a double($\sigma + \pi$)-aromatic molecule involving stronger π- than σ-aromatic component, in line with the shape of the $NICS_{zz}$-scan curve (Figure 9b). The calculation of the CMO-$NICS_{zz}$ values for the c-C_7 (C_{2v}) cluster showed that six σ-type MOs have positive $NICS_{zz}$ values of totally 122.6 ppm and the remaining eighteen MOs have negative $NICS_{zz}$ values of totally -154.9 ppm, thus rendering the c-C_7 (C_{2v}) cluster aromatic. The σ-type MOs (totally fifteen) contribute to diatropic CMO-$NICS_{zz}$ values by -118.3 ppm and the π-type MOs (HOMO-3,-4,-6) contribute to diatropic CMO-$NICS_{zz}$ values by -36.6 ppm. It is

evident that the net effect would be a stronger π- than σ-aromatic component as it is reflected on the shape of the NICS$_{zz}$-scan curve of c-C$_7$ (C_{2v}) cluster. It should be noticed that the NICS$_{zz}$-scan curve of c-C$_7$ (C_{2v}) cluster is similar to that of the benzene molecule. This could be understood on the basis of the CMO-NICS$_{zz}$ analysis data for benzene, which showed that five σ-type MOs have positive NICS$_{zz}$ values of totally 85.9 ppm and the remaining sixteen MOs have negative NICS$_{zz}$ values of totally -100.4 ppm. Among these MOs, nine σ-type MOs contribute to diatropic CMO-NICS$_{zz}$ values by -39.0 ppm and seven π-type MOs contribute to diatropic CMO-NICS$_{zz}$ values by -61.4 ppm. It is again evident that the net effect would be the dominant π-aromatic component for benzene.

3.7.3. The NICS$_{zz}$-scan curves and magnetotropicity of Fulvalene^{2-}, Phenalenyl^{+}, Oxazole, and [c-C$_8$H$_{24}$]$^{2+}$ molecules

Very recently Mills and Benish [91] evaluated the aromaticity of the tetrabenzo[5.5]fulvalene dianion through magnetic criteria and found that all rings exhibit appreciable aromaticity. The NICS$_{zz}$-scan curve (Figure 9c) justifies the aromaticity of the tetrabenzo[5.5]fulvalene dianion, indicating that it is totally due to the π-aromatic system.

The lowest T$_{x,y}$-allowed transitions of the tetrabenzo[5.5]fulvalene dianions are only of the π-type (Table 11). The same holds also true for the 12π electron phenalenyl cation which supports diatropic perimeter ring current. The NICS$_{zz}$-scan curve (Figure 9c) of the phenalenyl cation is typical for aromatic molecules exhibiting pure π-aromatic character. Very recently, Fowler *et al*. [92] using the ipsocentric approach predicted the diatropicity of the phenalenyl cation which arises mainly from the contribution of the doubly degenerate 2e HOMO-2 pair.

Table 11. Estimated excitation energies (in eV) of the lowest T$_{x,y}$- and R$_z$-allowed σ- and π-type transitions of selected aromatic organic molecules.

excitatic	Type	Excitation energies			
		Fulvalene^{2-}	Phenalenyl^{+}	Oxazole	[c-C$_8$H$_{24}$]$^{2+}$
$a \rightarrow b_2$	π-	**1.96**			
$b_2 \rightarrow b_1$	π-	**2.00**			
$a \rightarrow b_3$	π-	**2.69**			
$b_2 \rightarrow b_3$	π-R$_z$	2.10			
$e'' \rightarrow a_1''$	π-		**3.68**		
$e'' \rightarrow a_2''$	π-		**6.51**		
$a_2'' \rightarrow a_1''$	π-R$_z$		3.58		
$e_1' \rightarrow a_1'$	σ-		10.51		
$a_2' \rightarrow a_1'$	σ-R$_z$		11.75		
$a'' \rightarrow a''$	π-			6.64	
$a' \rightarrow a'$	σ-			8.52	
$e_u \rightarrow b_{1g}$	σ-				3.00
$e_u \rightarrow b_{2g}$	σ-				3.42

Morao and Cosio [25] applied a simple ring current model for describing the in-plane aromaticity in pericyclic reactions to oxazole, a five-membered π-aromatic heterocycle containing two heteroatoms. They found that this kind of aromatic compound can be described using two ring currents. The NICS$_{zz}$-

scan curve (Figure 9c) of oxazole in conjunction with the estimated excitation energies for the lowest $T_{x,y}$-allowed σ- and π-type transitions (Table 11) clearly indicate the double ($\sigma + \pi$)-aromatic character of oxazole involving stronger π- than σ-aromatic component.

Finally, both the shape of the $NICS_{zz}$-scan curve (Figure 9c) and the estimated excitation energies for the $T_{x,y}$-allowed transitions (Table 11) for the hypothetical $[c\text{-}C_8H_{24}]^{2+}$ species with delocalized electrons in a cyclic array of p orbitals arranged tangentially in σ-bonding fashion are in support of the pure σ-aromatic character in line with the ring-current maps calculated by Fowler *et al.* [93] It should be noted that the $[c\text{-}C_8H_{24}]^{2+}$ species correspond to a sixth order saddle point in the PES. The broadening of the $NICS_{zz}$-scan curve is what it is expected for an eigth-membered ring with $R_{av} = 3.072$ Å.

3.8. Predicting the peculiar aromaticity of borazine

Borazine, $c\text{-}B_3N_3H_6$ - the boron-nitrogen six-membered ring compound often referred to as "inorganic benzene - has been subject of controversial discussions with respect to the aromaticity of this molecule. Very recently Islas *et al.* [94] in their publication entitled *Borazine: to be or not to be aromatic* based on a detailed analysis of two molecular fields, the induced magnetic field ($\boldsymbol{B}^{ind}$) and the electron localization function (ELF) indicated that borazine can be described as a π-aromatic compound but it is not a globally aromatic species, since the delocalized system is not as homogeneous as that of benzene. The induced magnetic field in borazine is weaker than that of benzene but nevertheless pronounced and long-ranged. The $NICS_{zz}$-scan curve of borazine shown in Figure 10 clearly demonstrates the long-range π-aromaticity and the in-plane σ-antiaromaticity of borazine. It shows a maximum negative (diatropic) $NICS_{zz}$ value of -8.4 ppm at $z = 1.6$ Å above and below the ring and a maximum positive (paratropic) $NICS_{zz}$ value of 12.0 ppm at $z = 0$.

Figure 10. The $NICS_{zz}$-scan curve of the borazine molecule along with the molecular orbital energy level diagram, symmetries, 3D molecular orbital pictures and significant $T_{x,y}$- and R_z-allowed transitions leading to the diamagnetic and paramagnetic ring currents respectively, computed at the B3LYP/6-311+G(d,p) level.
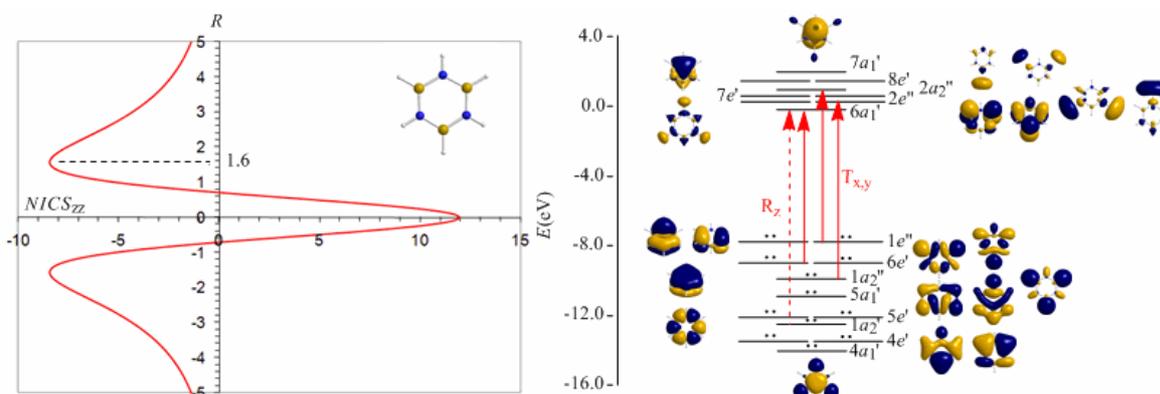
The estimated excitation energies of the lowest $T_{x,y}$-allowed transitions are for the π-type $e'' \rightarrow a_2''$ and $a_2'' \rightarrow e''$ excitations 8.57 eV and 10.19 eV respectively and for the σ-type $e' \rightarrow a_1'$ excitation 9.05

eV. The latter is outweighed by the $T_{x,y}$-allowed $a_2' \rightarrow a_1'$ transition with excitation energy 12.04 eV. The relatively high excitation energies lead to weak induced π-diatropic ring currents, which nicely explain the substantial decrease of the π-electron delocalization relative to benzene (compare the $NICS_{zz}^{max}$ values of -8.4 and -29.2 ppm, for the borazine and benzene molecules, respectively). It is interesting to notice that the local contributions of the σ electrons in borazine according to the calculations carried out by Islas *et al*. [94] generate a short-range response and a paratropic (antiaromatic) region in the center of the ring, while the π-orbital contribution to $\boldsymbol{B}^{ind}$ shows the typical response of an aromatic system. This is exactly the topology of the total ring currents represented by the $NICS_{zz}$-scan curve of borazine (Figure 10).

3.9.   Applying the magnetic NICS$_{zz}$-scan criterion to diagnose aromaticity/antiaromaticity in the non-planar corannulene, corannulene dianion and sumarene molecules

The bowl-shaped corannulene, $C_{20}H_{10}$, corannulene dianion, $[C_{20}H_{10}]^{2-}$ and sumarene, $C_{21}H_{12}$, polycyclic hydrocarbons, which share a fullerene substructure, have been studied extensively in recent years [95,96]. Such studies have emphasized the description of their aromaticity and electron interactions on curved surfaces from both the experimental and theoretical perspectives.

The counter-rotating ring currents in coronene and corannulene have been investigated by Jenneskens *et al*. [97] Very recently Monaco and Zanasi [98] calculated the π current of aromatic polycyclic hydrocarbons placed in a uniform magnetic field and found substantial localization on subunits in some cases. Moreover, Zanasi *et al*. [99] in their recent publication entitled *Magnetic Euripi in Corannulene* computed *ab initio* current densities for corannulene dianion, dication and tetraanion and found large π-ring currents with respect to benzene which undergo remarkable changes in response to variation in the oxidation state. The three corannulene ions along with the neutral species constitute a full set that spans all of the possible patterns of rim and hub circulations. Thus, for the neutral corannulene the magnetotropicity corresponds to paratropic/hub-diatropic/rim pattern, while for the corannulene dianion to diatropic/hub-paratropic/rim pattern.

The $NICS_{zz}$-scan curves of corannulene, corannulene dianion and sumanene computed for both the inner (hub) and outer (rim) rings are shown in Figure 11.

The $NICS_{zz}$-scan curve of the inner (hub) five-membered ring of corannulene clearly demonstrates the antiaromatic character of the ring (maximum $NICS_{zz}(0.2)$ value of 54.5 ppm) in line with the computed current-density maps for the σ, π, and total ($\sigma + \pi$) electrons at 1 a_0 above the molecular planes showing a paramagnetic counter-circulation on the inner hub [97-99]. The $NICS_{zz}$-scan curve of the inner (hub) five-membered ring of corannulene is similar to the $NICS_{zz}$-scan curve of the highly antiaromatic cross-conjugated annelated five-membered ring system, acepentalene, [45] corresponding to relatively narrow curve with half-band width of 1.3 Å. On the other hand, the $NICS_{zz}$-scan curve of the outer (rim) six-membered rings of corannulene exhibiting two maxima at a certain distance above and below the molecular plane and having $NICS_{zz}(0)$ value close to zero indicates their pure π-type aromatic character (minimum $NICS_{zz}(1.1)$ and $NICS_{zz}(-1.3)$ values of -24.1 and -17.1 ppm respectively), which is also consistent with the computed current-density maps showing a clear diamagnetic circulation around the outer rim [97-99]. It is important to be noticed that both the central

paramagnetic (paratropic) and the outer diamagnetic (diatropic) induced ring currents are enhanced inside the bowl but depleted on the outside as a result of ring current superpositions.

Figure 11. The $NICS_{zz}$-scan curves of corannulene, corannulene dianion and sumanene computed for both the inner (hub) and outer (rim) rings at the B3LYP/6-311+G(d,p) level.
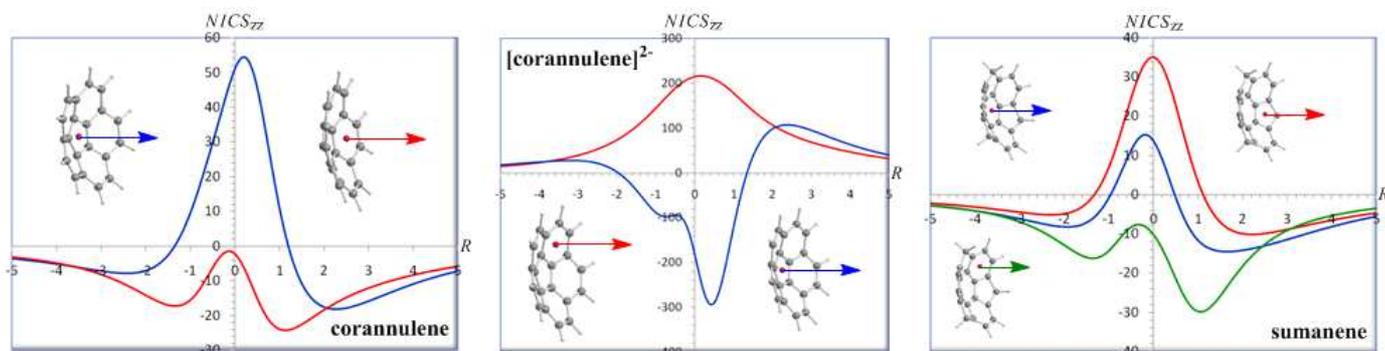
The $NICS_{zz}$-scan curve of the inner (hub) five-membered ring exhibiting two maxima at a certain distance above and below the molecular plane and having $NICS_{zz}(0)$ value close to zero clearly demonstrate the high π-aromaticity (diatropicity) of the hub (minimum $NICS_{zz}(0.4)$ value of -293.8 ppm). The $NICS_{zz}$-scan curve of the outer (rim) six-membered rings of corannulene dianion is typical of highly in-plane antiaromatic systems [45] (maximum $NICS_{zz}(0.2)$ value of 216.6 ppm). Notice again that the inner (hub) diamagnetic (diatropic) induced ring current is strongly enhanced inside the bowl but depleted on the outside. It is important to be noted that the $NICS_{zz}$-scan curves of corannulene and corannulene dianion correctly predict the paratropic/hub-diatropic/rim and diatropic/hub-paratropic/rim patterns respectively obtained by the *ab initio* computed probability current densities [99].

The $NICS_{zz}$-scan curve of the inner six-membered ring of sumanene indicates paratropicity at the ring center with a maximum $NICS_{zz}(-0.2)$ value of 15.3 ppm and a long range diatropicity with minimum $NICS_{zz}(1.7)$ and $NICS_{zz}(-1.9)$ values of -14.5 and -8.2 ppm respectively. Therefore the inner six-membered ring of sumanene can be considered practically as non aromatic. Notice again the enhancement of the induced diatropic ring currents inside the bowl. The $NICS_{zz}$-scan curve of the outer five-membered ring of sumanene (a typical curve for in-plane antiaromatic systems) [45] clearly illustrates the antiaromatic character of the ring, while the $NICS_{zz}$-scan curve of the outer six-membered ring of sumanene exhibiting two maxima at a certain distance above and below the molecular plane and having $NICS_{zz}(0)$ value close to 0 is characteristic of the pure π-aromaticity enhanced inside the bowl ($NICS_{zz}(1.1) = $ -29.8 ppm), but depleted on the outside ($NICS_{zz}(-1.4) = $ -16.2 ppm).

The 3D molecular orbital pictures of the MOs participating in the lowest $T_{x,y}$- and R_z-allowed transitions in corannulene, corannulene dianion and sumanene are shown in Figure 12.

Figure 12. 3D contour surfaces of the molecular orbitals participating in the lowest $T_{x,y}$- and R_z-allowed transitions of the corannulene, corannulene dianion and sumanene molecules.

LUMO+3 (a_2)	LUMO+2 (a_1)	LUMO+1 (e_1)	**LUMO** (e_1)	**HOMO** (e_1)	HOMO-1 (e_1)
-0.101	*-0.584*	*-1.983*		*-6.330*	*eV*

Corannulene (C_{5v})

LUMO+2 (a')	LUMO+1 (a'')	**LUMO** (a')	**HOMO** (a'')
5.407	*5.302*	*5.170*	*4.340 eV*

[Corannulene]$^{2-}$ (C_s)

L+2 (a_1)	L+1 (e)	**LUMO** (e)	**HOMO** (e)	H-1 (e)	H-2 (a_2)
-1.168	*-1.179*		*-5.832*	*-6.529*	*eV*

Sumanene (C_{3v})
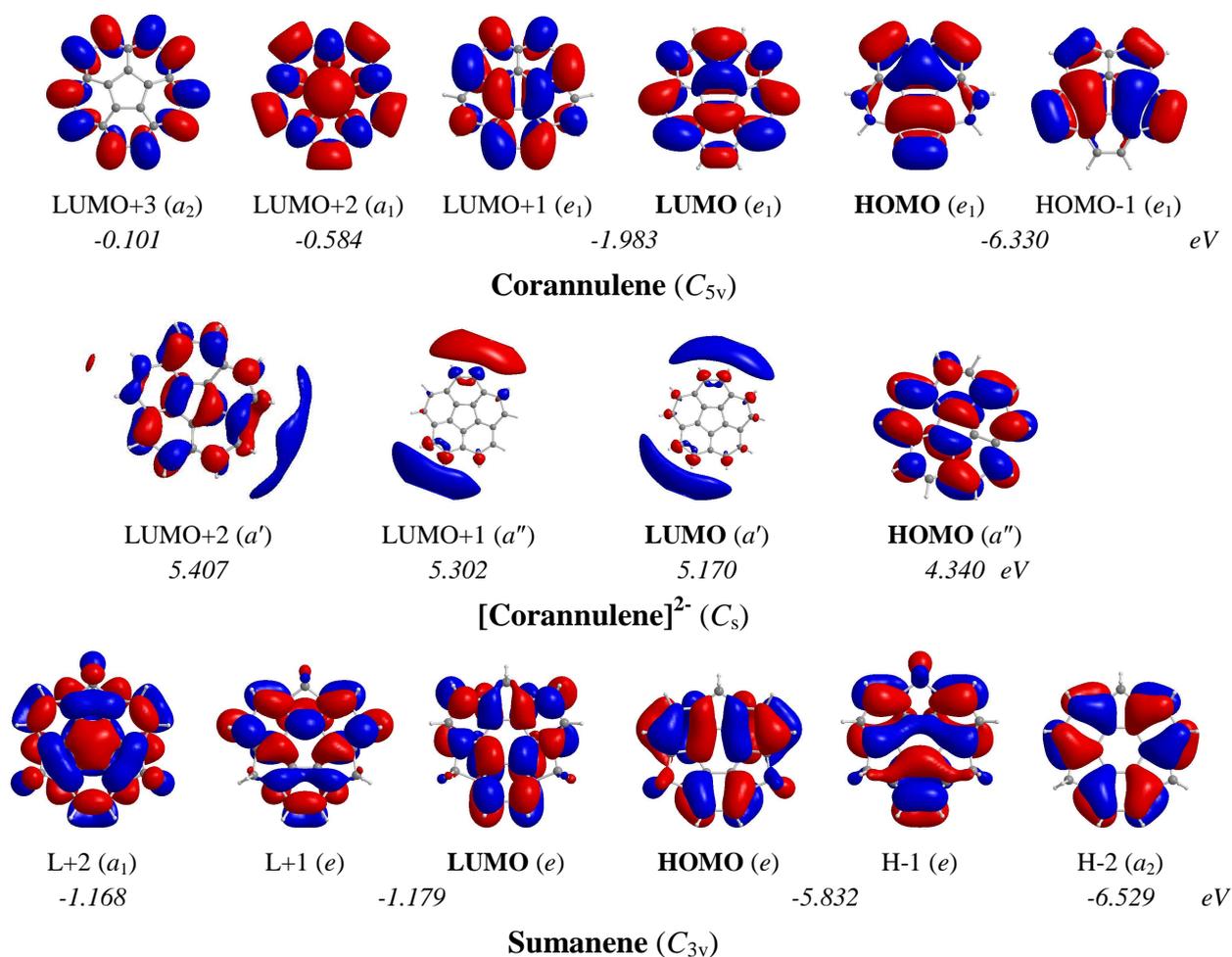
In the corannulene molecule with C_{5v} symmetry, the chief contribution to induced diatropic ring current arises from the $T_{x,y}$-allowed HOMO,-1 (e_1) → LUMO+2 (a_1) and HOMO,-1 (e_1) → LUMO+3 (a_2) transitions with excitation energies 5.75 and 6.23 eV respectively. On the other hand, the chief contribution to induced paratropic ring current arises from the R_z-allowed HOMO,-1 (e_1) → LUMO,+1 (e_1) transition with excitation energy 4.35 eV. For the corannulene dianion with C_s symmetry, the chief mixed contribution to induced paratropic and diatropic ring currents arises from the lowest R_z- and $T_{x,y}$-allowed HOMO (a'') → LUMO (a'), HOMO (a'') → LUMO+1 (a'') and HOMO (a'') → LUMO+2 (a') transitions with excitation energies 0.83, 0.96 and 1.07 eV respectively.

In the sumanene molecule with C_{3v} symmetry, the chief contribution to induced diatropic ring current arises from the lowest $T_{x,y}$-allowed HOMO,-1 (e) → LUMO+2 (a_1) transition with excitation energy 4.66 eV. Furthermore, the chief contribution to induced paratropic ring current arises from the lowest R_z-allowed HOMO,-1 (e) → LUMO,+1 (e) and HOMO-2 (a_2) → LUMO+2 (a_1) transitions with excitation energies 4.65 and 5.36 eV, respectively.

The estimated excitation energies of the lowest $T_{x,y}$- and R_z-allowed transitions of the corannulene, corannulene dianion and sumanene molecules in conjunction with the 3D molecular orbital pictures of

the relevant MOs account well for the magnetotropicity patterns derived from the shapes of the NICS$_{zz}$-scan curves.

4. Conclusions

To summarize, in the present computational study we showed that the NICS$_{zz}$-scan curves computed at the GIAO/B3LYP level in conjunction with symmetry-based selection rules provide efficient diagnostic tools of the orbital-type, σ-, π- and double ($\sigma + \pi$)- of aromaticity in a wide range of aromatic organic and main group inorganic rings.

Thus, the NICS$_{zz}$-scan curves of any aromatic molecule exhibiting pure σ-aromatic character are symmetric around the z-axis (perpendicular to the ring plane) with the NICS$_{zz}$ values decaying rapidly and monotically with respect to R and having a half-band width approximately less than 3 Å. This is the case of σ-aromatics exhibiting *s*-orbital aromaticity due to cyclic delocalization of two 1s electrons over the three-membered ring in $[c\text{-}H_3]^+$ and six 1*s* electrons over the four-, five- and six-membered rings in $[c\text{-}H_4]^{2-}$, $[c\text{-}H_5]^-$ and $[c\text{-}H_6]$ species, the $[c\text{-}B_3]^-$, $[c\text{-}B_3]^+$, $[c\text{-}B_2C]$, $[c\text{-}C_3]^{2+}$, $[c\text{-}B_4]$, $[c\text{-}B_4]^{2+}$, $[c\text{-}B_5]^+$ aromatics with in-plane σ-MOs of Hückel topology constructed from the overlap of the 2p AOs of the ring atoms, the $M_3(\mu_2\text{-}CO)_3(CO)_3$ (M = Ni, Pd, Pt) molecules, as well as for the transition states of the concerted transfer of two hydrogen atoms from ethane to ethylene (double group transfer reactions) and the trimerization of acetylene to form benzene, respectively. In all cases, the chief contribution to induced diatropic ring current arises from the lowest $T_{x,y}$-allowed occupied-to-unoccupied molecular orbital transitions involving exclusively σ-type molecular orbitals.; the estimated excitation energies accounting for the relative strength of their aromatic character.

A broad NICS$_{zz}$-scan curve with half-band width approximately > 3 Å is typical for double ($\sigma + \pi$)-aromatic molecules with comparable contribution to the induced total diatropic ring current from the σ- and π-diatropic ring currents. This is the case of a number of three-membered rings of main group atoms including the $[c\text{-}Be_3]^{2-}$, $[c\text{-}Mg_3]^{2-}$, $[c\text{-}E_3]^-$ (E = Al, Ga, In, Tl), $[c\text{-}E_3]^{2-}$ (E = C, Si, Ge), $[c\text{-}E_3]^+$ (E = N, P, As, Sb, Bi) and $[c\text{-}E_3]$ (E = S, Se, Te, Po), four-membered rings of main group atoms including the $[c\text{-}E_4]^{2-}$ (E = B, Al, Ga, In, Tl), $[c\text{-}Si_4]^{2+}$, $[c\text{-}Mg_4]^{2+}$ and $[c\text{-}Li_2Mg_2]$ and five-membered rings of main group atoms including the $[c\text{-}E_5]^-$ (E = N, P, As, Sb, Bi) and $[c\text{-}C_5H_5]^-$. The magnitude and type (σ-, π-) of the induced diatropic and paratropic ring currents are determined by the excitation energies of the lowest $T_{x,y}$- and R_z-allowed occupied $\rightarrow$ unoccupied molecular orbital transitions respectively with the coexistence of both the σ- and π-type transitions accounting well for the double ($\sigma + \pi$)-aromatic character of all these clusters.

The NICS$_{zz}$-scan curves exhibiting two maxima at a certain distance above and below the molecular plane are typical for double ($\sigma + \pi$)-aromatics where the π-diatropic ring current overwhelms the σ-type one. In the absence of any contribution from the σ-diatropic ring current the NICS$_{zz}$(0) value is close to zero and the molecule is a pure π-aromatic molecule. This is the case of a vast number of organic aromatic molecules. Again the estimated excitation energies of the lowest $T_{x,y}$- and R_z-allowed occupied $\rightarrow$ unoccupied molecular orbital transitions are indicative of the double ($\sigma + \pi$)-aromatic character of the organic aromatics accounting well for the observed varying σ-/π- ratio.

Finally, the NICS$_{zz}$-scan curves correctly predict the peculiar aromaticity of borazine and the magnetotropicity (diatropicity/paratropicity) patterns of the non-planar corannulene, corannulene dianion and sumanene.

References and Notes

1. Masui, H. Metalloaromaticity. *Coord. Chem. Rev.* **2001**, *219*, 957-992.
2. Tsipis, C.A. DFT study of "all-metal" aromatic compounds. *Coord. Chem. Rev.* **2005**, *249*, 2740-2762.
3. Boldyrev, A.I.; Wang, L.-S. All-metal aromaticity and antiaromaticity. *Chem. Rev.* **2005**, *105*, 3716-3757.
4. Wang, Y.; Robinson, G.H. Organometallics of the group 13 M-M bond (M = Al, Ga, In) and the concept of metalloaromaticity. *Organometallics* **2007**, *26*, 2-11.
5. Lee, V.Y.; Sekiguchi, A. Aromaticity of group 14 organometallics: Experimental aspects. *Angew. Chem. Int. Ed.* **2007**, *46*, 6596-6620.
6. Zubarev, D.Y.; Averkiev, B.B.; Zhai, H.-J.; Wang, L.-S.; Boldyrev, A.I. Aromaticity and antiaromaticity in transition-metal systems. *Phys. Chem. Chem. Phys.* **2008**, *10*, 257.
7. Schleyer, P.v.R., Guest Editor. Thematic Issue on Aromaticity, *Chem. Rev.* **2001**, *101*.
8. Schleyer, P.v.R., Guest Editor. Thematic Issue on Delocalization - Pi and Sigma. *Chem. Rev.* **2005**, *105*.
9. Special edition on New Perspectives on Aromaticity, *Phys. Chem. Chem. Phys.* **2004**, 6.
10. Mirkin, V.I.; Glukhotsev, M.N.; Simkin, B.Y. *Aromaticity and Antiaromaticity: Electronic and Structural Aspects*; John Wiley & Sons: New York, NY, USA, 1994.
11. Schleyer, P.v.R.; Maerker, C.; Dransfeld, A.; Jiao, H.; Hommes, N. J. R. V. Nucleus-independent chemical shifts: A simple and efficient aromaticity probe. *J. Am. Chem. Soc.* **1996**, *118*, 6317-6318.
12. Schleyer, P.v.R.; Manohran, M.; Wang, Z.-X.; Kiran, B.; Jiao, H.; Puchta, R.; Hommes, N.J.R.V.R. Dissected nucleus-independent chemical shift analysis of pi-aromaticity and antiaromaticity. *Org. Lett.* **2001**, *3*, 2465-2468.
13. Chen, Z.; Wannere, C.S.; Corminboeuf, C.; Puchta, R.; Schleyer, P.v.R. Nucleus-independent chemical shifts (NICS) as an aromaticity criterion. *Chem. Rev.* **2005**, *105*, 3842-3888.
14. Klod, S.; Kleinpeter, E. *Ab initio* calculation of the anisotropy effect of multiple bonds and the ring current effect of arenes - application in conformational and configurational analysis. *J. Chem. Soc. Perkin Trans.* **2001**, *2*, 1893-1898.
15. Fallah-Bagher-Shaidaei, H.; Wannere, C.S.; Corminboeuf, C.; Puchta, R.; Schleyer, P.v.R. Which NICS aromaticity index for planar pi rings is best? *Org. Lett.* **2006**, *8*, 863-866.
16. Wodrich, M.D.; Corminboeuf, C.; Park, S.S.; Schleyer, P.v.R. Double aromaticity in monocyclic carbon, boron, and borocarbon rings based on magnetic criteria. *Chem. Eur. J.* **2007**, *13*, 4582-4593.
17. Bohmann, J.A.; Weinhold, F.; Farrar, T.C. Natural chemical shielding analysis of nuclear magnetic resonance shielding tensors from gauge- including atomic orbital calculations. *J. Chem. Phys.* **1997**, *107*, 173.

18. Corminboeuf, C.; Heine, T.; Weber, J. Evaluation of aromaticity: A new dissected NICS model based on canonical orbitals *Phys. Chem. Chem. Phys.* **2003**, *5*, 246-251.

19. Heine, T.; Schleyer, P.v.R.; Corminboeuf, C.; Seifert, G.; Reviakine, R.; Weber, J. Analysis of aromatic delocalization: Individual molecular orbital contributions to nucleus-independent chemical shifts. J. *Phys. Chem. A* **2003**, *107*, 6470-6475.

20. Stanger, A. Nucleus-independent chemical shifts (NICS): Distance dependence and revised criteria for aromaticity and antiaromaticity *J. Org. Chem.* **2006**, *71*, 883.

21. Stanger, A. Can substituted cyclopentadiene become aromatic or antiaromatic? *Chem. Eur. J.* **2006**, *12*, 2745-2751.

22. Poater, J.; Bofill, J.M.; Alemany, P.; Solà, M. Role of electron density and magnetic couplings on the nucleus-independent chemical shift (NICS) profiles of [2.2]paracyclophane and related species. *J. Org. Chem.* **2006**, *71*, 1700-1702.

23. Jiménez-Halla, J.O.C.; Matito, E.; Robles, J.; Solà, M. Nucleus-independent chemical shift (NICS) profiles in a series of monocyclic planar inorganic compounds. *J. Organometal. Chem.* **2006**, *691*, 4359-4366.

24. Seal, P; Chakrabarti, S. Is nucleus-independent chemical shift scan a reliable aromaticity index for planar heteroatomic ring systems? *J. Phys. Chem. A* **2007,** *111*, 9988-9994.

25. Morao, I; Cossio, F.P. A simple ring current model for describing in-plane aromaticity in pericyclic reactions. *J. Org. Chem.* **1999**, *64*, 1868-1874.

26. Data, A.; Mallajosyula, S.S.; Pati, S.K. Nonlocal electronic distribution in metallic clusters: A critical examination of aromatic stabilization. *Acc. Chem. Res.* **2007,** *40*, 213-221.

27. Datta, A.; Pati, S.K. Limit to puckering of benzene with sterically crowded molecules: Hexaferrocenylbenzene. *Chem. Phys. Lett.* **2006,** *433*, 67-70.

28. Datta, A.; Pati, S.K. Rationalization of the pi-sigma (anti)aromaticity in all metal molecular clusters. *J. Chem. Theory Comput.* **2005**, *1*, 824-826.

29. Datta, A.; Pati, S.K. Stable transition metal complexes of an all-metal antiaromatic molecule (Al_4Li_4): Role of complexations. *J. Am. Chem. Soc.* **2005**, *127*, 3496-3500.

30. Steiner, E.; Fowler, P.W. Four- and two-electron rules for diatropic and paratropic ring currents in monocyclic pi systems. *Chem. Commun.* **2001**, 2220-2221.

31. Steiner, E.; Fowler, P.W. Patterns of ring currents in conjugated molecules: A few-electron model based on orbital contributions. *J. Phys. Chem. A* **2001**, *105*, 9553-9562.

32. Fowler, P.W.; Steiner, E.; Havenith, R.W.A.; Jenneskens, L.W. Current density, chemical shifts and aromaticity. *Magn. Reson. Chem.* **2004**, *42*, S68-S78.

33. Corminboeuf, C.; King, R.B.; Schleyer, P.v.R. Implications of molecular orbital symmetries and energies for the electron delocalization of inorganic clusters. *ChemPhysChem* **2007**, *8*, 391-398.

34. Soncini, A.; Teale, A.M.; Helgaker, T.; De Proft, F.; Tozer, D.J. Maps of current density using density-functional methods. *J. Chem. Phys.* **2008**, *129*, 074101.

35. Viglione, R.G.; Zanasi, R.; Lazzeretti, P. Are ring currents still useful to rationalize the benzene proton magnetic shielding? *Org. Lett.* **2004**, *6*, 2265-2267.

36. Pelloni, S.; Faglioni, F.; Zanasi, R.; Lazzeretti, P. Topology of magnetic-field-induced current-density field in diatropic monocyclic molecules. *Phys. Rev.* **2006**, *74*, 012506.

37. Jusélius, J.; Sundholm, D. *Ab initio* determination of the induced ring current in aromatic molecules. *Phys. Chem. Chem. Phys.* **1999**, *1*, 3429-3435.

38. Jusélius, J.; Sundholm, D.; Gauss, J. Calculation of current densities using gauge-including atomic orbitals. *J. Chem. Phys.* **2004**, *121*, 3952-3963.

39. Lin, Y.-C.; Jusélius, J.; Sundholm, D.; Gauss, J. Magnetically induced current densities in Al_4^{2-} and Al_4^{4-} species studied at the coupled-cluster level *J. Chem. Phys.* **2005**, *122*, 214308.

40. Merino, G.; Heine, T.; Seifert, G. The induced magnetic field in cyclic molecules. *Chem. Eur. J.* **2004**, *10*, 4367-4371.

41. Heine, T.; Islas, R.; Merino, G. sigma and pi contributions to the induced magnetic field: Indicators for the mobility of electrons in molecules. *J. Comput. Chem.* **2007**, *28*, 302-309.

42. Periyasamy, G.; Burton, N.A.; Hillier, I.H.; Thomas, J.M.H. Electron delocalization in the metallabenzenes: A computational analysis of ring currents. *J. Phys. Chem. A* **2008**, *112*, 5960-5972.

43. Geuenich, D.; Hess, K.; Kohler, F.; Herges, R. Anisotropy of the induced current density (ACID), a general method to quantify and visualize electronic delocalization. *Chem. Rev.* **2005**, *105*, 3758-3772.

44. Tsipis, A.C.; Depastas, I.G.; Karagiannis E.E.; Tsipis, C.A. Diagnosis of Magnetoresponsive Aromatic and Antiaromatic Zones in Three-Membered Rings of *d*- and *f*-Block Elements. *J. Comput. Chem.* **2009**, DOI: 10.1002/jcc21327

45. Tsipis, A.C. Efficiency of the $NICS_{zz}$-scan Curves to Probe the Antiaromaticity of Organic and Inorganic Rings/Cages. *Phys. Chem. Chem. Phys.* **2009**, *11*, 8244-8261.

46. Frisch, M.J.; Schlegel, H.B.; Scusseria, G.E.; Robb, M.A.; Cheeseman, J.R.; Zakrzewski, V.G.; Montgomery, J.A.; Vreven, T.; Kudin, K.N.; Burant, J.C.; Millan, J.M.; Iyengar, S.S.; Tomasi, J.; Barone, V.; Mennucci, B.; Cossi, M.; Scalmani, G.; Rega, N.; Petersson, G.A.; Nakatsuji, H.; Hada, M.; Ehara, M.; Toyota, K.; Fukuda. R.; Hasegawa, J.; Ishida, M.; Nakajima, T.; Honda, Y.; Kitao, O.; Nakai, H.; Klene, M.; Li, X.; Knox, J.E.; Hratchian, H.P.; Cross, J.B.; Adamo, C.; Jaramillo, J.; Gomperts, R.; Stratmann, R.E.; Yazyev, O.; Austin, A J.; Cammi, R.; Pomelli, C.; Ochterski, J.W.; Ayala, P.Y.; Morokuma, K.; Voth, G.A.; Salvador, P.; Dannenberg, J.J.; Zakrzewski, V.G.; Dapprich, S.; Daniels, A.D.; Strain, M.C.; Farkas, O.; Malick, D.K.; Rabuck, A.D.; Raghavachari, K.; Foresman, J.B.; Ortiz, J.V.; Cui, Q.; Baboul, A.G.; Clifford, S.; Cioslowski, J.; Stefanov, B.B.; Liu, G.; Liashenko, A.; Piskorz, P.; Komaromi, I.; Martin, R.L.; Fox, D.J.; Keith, T.; Al-Laham, M.A.; Peng, C.Y.; Nanayakkara, A.; Challacombe, M.; Gill, P.M.W.; Johnson, B.; Chen, W.; Wong, M.W.; Gonzalez, C.; Pople, J.A. *Gaussian 03, Revision E. 01*; Gaussian, Inc.: Pittsburgh, PA, USA, 2004.

47. Dolg, M.; Stoll, H.; Preuss, H.; Pitzer, R. M. Relativistic and correlation-effects for element 105 (Hahnium, Ha) - A comparative-study of M and MO (M = Nb, Ta, Ha) using energy-adjusted *ab initio* pseudopotentials. *J. Phys. Chem.* **1993**, *97*, 5852-5859.

48. Stuttgart RSC 1997 ECP EMSL Basis Set Exchange Library, https://bse.pnl.gov/bse/portal, accessed on 9 June 2008.

49. Schlegel, H.B. Optimization of equilibrium geometries and transition structures. *J. Comput. Chem.,* **1982**, *3*, 214-218.

50. Ditchfield, R.D. Self-consistent perturbation theory of diamagnetism I. A gauge-invariant LCAO method for N.M.R. chemical shifts. *Mol. Phys.* **1974**, *27*, 789-807.

51. Gauss, J. Effects of electron correlation in the calculation of nuclear-magnetic-resonance chemical-shifts. *J. Chem. Phys.* **1993**, *99*, 3629-3643.

52. Jiao, H.; Schleyer, P.v.R.; Glukhovtsev, M.N. Are the D_{mh} symmetric H_x^q rings with 4n+2 sigma-electrons and hydrogen clusters aromatic? *J. Phys. Chem.* **1996**, *100*, 12299-12304.

53. Jursic, S.B. Hybrid density functional theory study of hydrogen cluster aromaticity by computing their relative energies and magnetic properties. *Int. J. Quantum Chem.* **1999**, *73*, 451-458.

54. Havenith, R.W.A.; De Proft, F.; Fowler, P.W.; Geerlings, P. sigma-Aromaticity in H_3^+ and Li_3^+: Insights from ring-current maps. *Chem. Phys. Lett.* **2005**, *407*, 391-396.

55. Yong, L.; Wu, S.D.; Chi, X.X. Theoretical study of aromaticity in small hydrogen and metal cation clusters X_3^+ (X = H, Li, Na, K, and Cu). *Int. J. Quantum Chem.* **2007**, *107*, 722-728.

56. Kuznetsov, A.E.; Boldyrev, A.I. Theoretical evidence of aromaticity in X_3^- (X = B, Al, Ga) species. *Struct. Chem.* **2002**, *13*, 141-148.

57. Zhai, H.-J.; Wang, L.-S.; Alexandrova, A.N.; Boldyrev, A.I.; Zakrzewski, V.G. Photoelectron spectroscopy and *ab initio* study of B_3^- and B_4^- anions and their neutrals. *J. Phys. Chem. A* **2003**, *107*, 9319-9328.

58. Alexandrova, A.N.; Boldyrev, A.I.; Zhai, H.-J.; Wang, L.-S. All-boron aromatic clusters as potential new inorganic ligands and building blocks in chemistry. *Coord. Chem. Rev.* **2006**, *250*, 2811-2866 and references therein.

59. Fernández, I.; Sierra, M.A.; Cossio, F.P. In-plane aromaticity in double group transfer reactions. *J. Org. Chem.* **2007**, *72*, 1488-1491.

60. Morao, I.; Lecea, B.; Cossio, F.P. In-plane aromaticity in 1,3-dipolar cycloadditions. *J. Org. Chem.* **1997**, *62*, 7033-7036.

61. Jiao, H.; Schleyer, P.v.R. Aromaticity of pericyclic reaction transition structures: magnetic evidence. *J. Phys. Org. Chem.* **1998**, *11*, 655-662.

62. Scheschkewitz, D.; Hofmann, M.; Ghaffari, A.; Amseis, P.; Praesang, C.; Mesbah, W.; Geiseler, G.; Massa, W.; Berndt, A. Very strong anionic homoaromaticity in (deloc-1,3,4)-1-sila-3,4-diboracyclopentane-1-ides, the importance of the energy of the reference system for homoaromatic stabilization energies. *J. Organomet. Chem.* **2002**, *646*, 262-270.

63. Alexandrova, A.N.; Boldyrev, A.I. sigma-aromaticity and sigma-antiaromaticity in alkali metal and alkaline earth metal small clusters. *J. Phys. Chem. A* **2003**, *107*, 554-560.

64. Fowler, P.W.; Baker, J.; Lillington M. The ring current in cyclopropane. *Theor. Chem. Acc.* **2007**, *118*, 123-127.

65. Pelloni, S.; Lazzeretti, P.; Zanasi, R. Assessment of sigma-diatropicity of the cyclopropane molecule. *J. Phys. Chem. A* **2007**, *111,* 8163-8169.

66. Wu, W.; Ma, B.; Wu, J.I-C.; Schleyer, P.v.R.; Mo, Y. Is cyclopropane really the σ-aromatic paradigm? *Chem. Eur. J.* **2009**, *15*, 9730-9736.

67. King, R.B. Metal cluster topology. 21. Sigma aromaticity in triangular metal carbonyl clusters. *Inorg. Chim. Acta* **2003**, *350*, 126-130.

68. Corminboeuf, C.; Schleyer, P.v.R.; King, R.B. Aromaticity of tri- and tetranuclear metal-carbonyl clusters based on magnetic criteria. *Chem. Eur. J.* **2007**, *13*, 978-984.

69. Jimenez-Halla, J.O.C.; Matito, E.; Blancafort, L.; Robles, J.; Sola, M. Tuning Aromaticity in Trigonal Alkaline Earth Metal Clusters and Their Alkali Metal Salts. *J. Comput. Chem.* **2009**, DOI: 10.1002/jcc.2191.

70. Kuznetsov, A.E.; Boldyrev, A.I. A single pi-bond captures 3, 4 and 5 atoms. *Chem. Phys. Lett.* **2004**, *388*, 452-456.

71. Zhan, C.-G.; Zheng, F.; Dixon, D.A. Electron affinities of Al_n clusters and multiple-fold aromaticity of the square Al_4^{2-} structure. *J. Am. Chem. Soc.* **2002**, *124*, 14795-14803.

72. Li, Z.-H.; Moran, D.; Fan, K.-N.; Schleyer, P.v.R. sigma-Aromaticity and sigma-antiaromaticity in saturated inorganic rings. *J. Phys. Chem. A* **2005**, *109*, 3711-3716.

73. Li, X.; Kuznetsov, A.E.; Zhang, H.-F.; Boldyrev, A.I.; Wang, L.-S. Observation of All-Metal Aromatic Systems. *Science* **2001**, *291*, 859.

74. Islas, R.; Heine, T.; Merino, G. sigma and pi contributions to the induced magnetic field: Indicators for the mobility of electrons in molecules. *J. Chem. Theory Comput.* **2007**, *3*, 302-309.

75. Juselius, J.; Straka, M.; Sundholm, D. Magnetic-shielding calculations on Al_4^{2-} and Analogues. A new family of aromatic molecules? *J. Phys. Chem. A* **2001**, *105*, 9939-9944.

76. Fowler, P.W.; Havenith, R.W.A.; Steiner, E. Unconventional ring currents in an 'all-metal aromatic', Al_4^{2-}. *Chem. Phys. Lett.* **2001**, *342*, 85-90.

77. Fowler, P.W.; Havenith, R.W.A.; Steiner, E. Ring current and electron delocalisation in an all-metal cluster, Al_4^{2-}. *Chem. Phys. Lett.* **2002**, *359*, 530-536.

78. Havenith, R.W.A.; Fowler, P.W.; Steiner, E.; Shetty, S.; Kanhere, D.; Pal, S. Aromaticity and antiaromaticity of Li_xAl_4 clusters: Ring current patterns *versus* electron counting. *Phys. Chem. Chem. Phys.* **2004**, *6*, 285-288.

79. Havenith, R.W.A.; Fowler, P.W. The origin of the ring current in the all-metal aromatic, Al_4^{2}. *Phys. Chem. Chem. Phys.* **2006**, *8*, 3383-3386.

80. Chen, Z.; Corminboeuf, C.; Heine, T.; Bohmann, J.; Schleyer, P.v.R. Do all-metal antiaromatic clusters exist? *J. Am. Chem. Soc.* **2003**, *125*, 13930-13931.

81. Boldyrev, A.I.; Kuznetsov, A.E. On the resonance energy in new all-metal aromatic molecules. *Inorg. Chem.* **2002**, *41*, 532-537.

82. Havenith, R.W.A.; van Lenthe, J.H.A valence bond study of the sigma and pi aromatic species Al_4^{2-}. *Chem. Phys. Lett.* **2004**, *385*, 198-201.

83. Santos, J.C.; Tiznado, W.; Conteras, R.; Fuentealba, Sigma-pi separation of the electron localization function and aromaticity. *J. Chem. Phys.* **2004**, *120*, 1670-1673.

84. Chattaraj, P.K.; Roy, D.R.; Elango, M.; Subramanian V. Chemical reactivity descriptor based aromaticity indices applied to Al_4^{2-} and Al_4^{4-} systems. *J. Mol. Struct.(THEOCHEM)* **2006**, *759*, 109-110.

85. Mandado, M.; Krishtal, A.; van Alensoy, C.; Bultinck, P.; Hermida-Ramon, J. M. Bonding study in all-metal clusters containing Al_4 units. *J. Phys. Chem. A* **2007**, *111*, 11885-11893.

86. Zhai, H.-J.; Wang, L.-S.; Kuznetsov, A.E.; Boldyrev, A.I. Probing the electronic structure and aromaticity of pentapnictogen cluster anions Pn_5^- (Pn = P, As, Sb, and Bi) using photoelectron spectroscopy and *ab initio* calculations. *J. Phys. Chem. A* **2002**, *106*, 5600-5606.

87. De Proft, F.; Fowler, P.W.; Havenith, W.A.; Schleyer, P.v.R.; van Lier, G.; Geerlings, P. Ring Currents as Probes of the Aromaticity of Inorganic Monocycles : P_5^-, As_5^-, S_2N_2, $S_3N_3^-$, $S_4N_3^+$, $S_4N_4^{2+}$, $S_5N_5^+$, S_4^{2+} and Se_4^{2+}. *Chem. Eur. J.* **2004**, *10*, 940-950.

88. Lambrecht, D.S.; Fleig, T.; Sommerfeld, T. Instability of the Al-4(2-) "All-Metal aromatic" ion and its implications. *J. Phys. Chem. A* **2008**, *112*, 2855-2862.

89. De Proft, F.; Schleyer, P.v.R.; van Lenthe, J.H.; Stahl, F.; Geerlings, P. Magnetic properties and aromaticity of o-, m-, and p-benzyne. *Chem. Eur. J.* **2002**, *8*, 3402-3410.

90. Hofmann, M.; Berndt, A. (pi+sigma)-double aromatic and pi,sigma-mixed aromatic boron compounds with two electrons delocalized over three centers. *Heteroatom. Chem.* **2006**, *17*, 224-237.

91. Mills, N.S.; Benish, M. The aromaticity/antiaromaticity continuum. 1. Comparison of the aromaticity of the dianion and the antiaromaticity of the dication of tetrabenzo[5.5]fulvalene via magnetic measures. *J. Org. Chem.* **2006**, *71*, 2207-2213.

92. Cryański, M.K.; Havenith, R.W.A.; Dobrowolski, M.A.; Gray, B.R.; Krygowski, T.M.; Fowler, P.W.; Jenneskens, L.W. The phenalenyl motf: A magnetic chameleon. *Chem. Eur. J.* **2007**, *13*, 2201-2207.

93. Fowler, P.W.; Rogowska, A.; Soncini, A.; Lillington, M.; Olson, L. P. Currents in tangentially p-p bonded sigma-aromatic systems. *J. Org. Chem.* **2006**, *71*, 6459-6467.

94. Islas, R.; Chamorro, E.; Robles, J.; Heine, T.; Santos, J.C.; Merino, G. Borazine: to be or not to be aromatic. *Struct. Chem.* **2007**, *18*, 833-839.

95. Wu, Y.-T.; Siegel, J.S. Aromatic Molecular-Bowl Hydrocarbons: Synthetic Derivatives, Their Structures, and Physical Properties. *Chem. Rev.* **2006**, *106*, 4833-4867.

96. Tsefrikas, V.M.; Scott, L.T. Geodesic Polyarenes by Flash Vacuum Pyrolysis. *Chem. Rev.* **2006**, *106*, 4868-4884.

97. Steiner, E.; Fowler, P.W.; Jenneskens L.W. Counter-Rotating Ring Currents in Coronene and Corannulene. . *Angew. Chem. Int. Ed.* **2001**, *40*, 362-366.

98. Monaco, G.; Zanasi, R. On the additivity of current density in polycyclic aromatic hydrocarbons. *J. Chem. Phys.* **2009**, *131*, 044126-044135.

99. Monaco, G.; Scott, L.T.; Zanasi, R. Magnetic Euripi in Corannulene. *J. Phys. Chem.* **2008**, *112*, 8136-8147.